stichting
mathematisch
centrum

MC

AFDELING NUMERIEKE WISKUNDE
(DEPARTMENT OF NUMERICAL MATHEMATICS)

NW 114/81 OKTOBER

W.J.A. MOL

# COMPUTATION OF FLOWS AROUND A KARMAN-TREFFTZ PROFILE

Preprint

kruislaan 413 1098 SJ amsterdam

*Printed at the Mathematical Centre, 413 Kruislaan, Amsterdam.*

*The Mathematical Centre, founded the 11-th of February 1946, is a non-profit institution aiming at the promotion of pure mathematics and its applications. It is sponsored by the Netherlands Government through the Netherlands Organization for the Advancement of Pure Research (Z.W.O.).*

---

1980 Mathematics subject classification: 65N05, 65N20, 65F10

---

# Computation of flows around a Karman-Trefftz profile*)

by

W.J.A. Mol

ABSTRACT

In this report we consider the stationary Navier-Stokes equations in $\omega - \psi$ formulation. The equations are discretized with Il'in's method and Newton-linearized. Each linear system is solved by the multigrid method.

Il'in's method induces artificial viscosity, especially in regions with large 2nd derivatives of the vorticity (e.g. in boundary layers). To reduce this artificial viscosity mesh refinement is applied in those regions.

The flows in a square cavity and around a cylinder are computed. These are test problems for a more practical problem: the flow around a Karman-Trefftz profile, which is also computed.

KEY WORDS & PHRASES: *Il'in's method, Newton linearization, multigrid method, mesh refinement*

---

*) This report will be submitted for publication elsewhere.

CONTENTS

# 1. INTRODUCTION

In MOL [5] a multigrid method is proposed which is efficient and robust i.e. the method is not only fast for the Poisson equation but also for the anisotropic diffusion and convection diffusion equations for small values of the perturbation parameter.

This multigrid method, from now on called *MULGRI* uses 7-point ILU decomposition as smoothing operator, Galerkin approximation as coarse grid operator, 7-point prolongation and restriction, 1 coarse grid correction, no smoothing before and 1 smoothing step after correction. More theoretical arguments for the choice of these parameters and operators can be found in MOL [6].

*MULGRI* is also efficient for problems with variable coefficients and non-linear problems (see MOL [4]). In all these cases the number of operations is O(N), with N the number of grid points. The number of operations for 0.1 reduction of the residual is 19N for the Poisson equation. This number is even smaller, when we exploit the fact that the coefficients in the Poisson case are constant.

Two flow problems are solved by *MULGRI* in MOL [7]: the stationary Navier-Stokes equations in a square cavity and around a cylinder. *MULGRI* is also efficient and robust for these problems.

In this report we go into the problem of solving the stationary Navier-Stokes equations more extensively. We also look at flows around a slender body with mesh refinement.

In chapter 2 the stationary Navier-Stokes equations are considered in $\omega - \psi$ formulation. The equations are discretized with Il'in's method and the discretized system is Newton linearized. The stream function and vorticity equations are solved simultaneously after application of conform mapping and mesh refinement.

In chapter 3 *MULGRI* is adapted to the 2 variables case.

In chapter 4 and 5 the flows in a square cavity and around a cylinder are computed respectively.

In chapter 6 and 7 we compute the flow around a Karman-Trefftz profile with mesh refinement in boundary layer and wake. By choosing a suitable mesh refinement the artificial viscosities are reduced for large Reynolds numbers.

## 2. THE NAVIER-STOKES EQUATIONS

### 2.1. Coordinate transformations

Consider the Navier-Stokes (NS) equations in $\omega - \psi$ formulation:

$$(2.1.1) \qquad \begin{cases} \Delta_{xy}\,\psi = \omega \\ \dfrac{\partial(\psi,\omega)}{\partial(y,x)} = \dfrac{1}{Re}\,\Delta_{xy}\omega \end{cases} \qquad (x,y) \in \Omega^*$$

with $\Delta_{xy} = \dfrac{\partial^2 .}{\partial x^2} + \dfrac{\partial^2 .}{\partial y^2}$ and $\dfrac{\partial(\psi,\omega)}{\partial(y,x)} = \dfrac{\partial\psi}{\partial y}\dfrac{\partial\omega}{\partial x} - \dfrac{\partial\omega}{\partial x}\dfrac{\partial\omega}{\partial y}$. Re is the Reynolds number of the problem.

2 coordinate transformations are applied: a conformal transformation $\xi' = \xi'(x,y)$ and $\eta' = \eta'(x,y)$ and a coordinate stretching $\xi = \xi(\xi')$ and $\eta = \eta(\eta')$. The NS-equations after these transformations are:

$$(2.1.2) \qquad \begin{cases} A\dfrac{\partial}{\partial\xi}\left(A\dfrac{\partial\psi}{\partial\xi}\right) + B\dfrac{\partial}{\partial\xi}\left(B\dfrac{\partial\psi}{\partial\eta}\right) = M\omega \\ AB\dfrac{\partial(\psi,\omega)}{\partial(\eta,\xi)} = \dfrac{1}{Re}\left\{A\dfrac{\partial}{\partial\xi}\left(A\dfrac{\partial\omega}{\partial\xi}\right) + B\dfrac{\partial}{\partial\eta}\left(B\dfrac{\partial\omega}{\partial\xi}\right)\right\} \end{cases} \qquad (\xi,\eta) \in \Omega$$

with

$$(2.1.3) \qquad \begin{cases} M = \left\{\left(\dfrac{\partial\xi'}{\partial x}\right)^2 + \left(\dfrac{\partial\xi'}{\partial y}\right)^2\right\}^{-1} \\ A = \dfrac{d\xi}{d\xi'}\,, \quad B = \dfrac{d\eta}{d\eta'}\,. \end{cases}$$

These equations represent the most general form of the NS-equations in this report. $\Omega$ will be the square $\Omega = (0,H) \times (0,H)$, $H \in \mathbb{R}$.

### 2.2. Discretization

System (2.1.2) is discretized on a rectangular grid $\Omega^{\ell}$, which has uniform mesh size in both directions:

$$(2.2.1)\qquad \begin{cases} \Omega^{\ell} = \{(\xi_i,\eta_j) \mid \xi_i = (i+1)h,\ \eta_j = (j+1)h,\ i = 0(1)2^{\ell}, \\ \qquad\qquad\qquad\qquad\qquad\qquad\qquad\qquad\qquad\qquad j = 0(1)2^{\ell}\} \\ h = H/(2^{\ell} + 2) \end{cases}$$

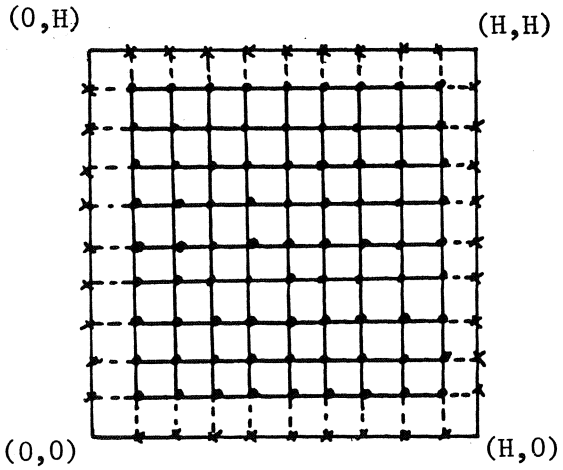


Figure 2.2.1 Grid $\Omega^3$ (the dots) and the boundary points $\partial\Omega^3$ (the crosses)

Note that $\Omega^{\ell}$ lies a distance h within the boundary $\partial\Omega$ of $\Omega$. This is because the boundary conditions of the NS-equations are substituted in the difference scheme. The boundary conditions are discretized in the grid points:

$$(2.2.2)\qquad \begin{cases} \partial\Omega_1^{\ell} = \{(H,\eta_j) \mid \eta_j = (j+1)h, \quad j = 0(1)2^{\ell}\} \\ \partial\Omega_2^{\ell} = \{(\xi_i,H) \mid \xi_i = (i+1)h, \quad i = 0(1)2^{\ell}\} \\ \partial\Omega_3^{\ell} = \{(0,\eta_j) \mid \eta_j = (j+1)h, \quad j = 0(1)2^{\ell}\} \\ \partial\Omega_4^{\ell} = \{(\xi_i,0) \mid \xi_i = (i+1)h, \quad i = 0(1)2^{\ell}\} \\ \partial\Omega^{\ell} = \partial\Omega_1^{\ell} \cup \partial\Omega_2^{\ell} \cup \partial\Omega_3^{\ell} \cup \partial\Omega_4^{\ell} \end{cases}$$

The 2nd derivative of $\psi$ in $\xi$-direction is discretized by central differences:

$$(2.2.3)\qquad A\frac{\partial}{\partial\xi}\left(A\frac{\partial\psi}{\partial\xi}\right)\Big|_{i,j} \cong \frac{1}{\bar{h}_i}\left\{\frac{\psi_{i+1,j}}{h_i} - \left(\frac{1}{h_i}+\frac{1}{h_{i-1}}\right)\psi_{i,j} + \frac{\psi_{i-1,j}}{h_{i-1}}\right\},$$

with

$$(2.2.4)\qquad h_{i-1} = \frac{h}{A_{i-\frac{1}{2}}}\,,\quad h_i = \frac{h}{A_{i+\frac{1}{2}}}\,,\quad \bar{h}_i = \frac{h}{A_i}\,.$$

The 2nd derivative of $\psi$ in $\eta$-direction is approximated by:

$$(2.2.5)\qquad B\frac{\partial}{\partial\eta}\left(B\frac{\partial\psi}{\partial\eta}\right)\Big|_{i,j} \cong \frac{1}{\bar{h}_j}\left\{\frac{\psi_{i,j+1}}{h_j} - \left(\frac{1}{h_j}+\frac{1}{h_{j-1}}\right)\psi_{ij} + \frac{\psi_{i,j-1}}{h_{j-1}}\right\},$$

with

$$(2.2.6)\qquad h_{j-1} = \frac{h}{B_{j-\frac{1}{2}}}\,,\quad h_j = \frac{h}{B_{j+\frac{1}{2}}}\,,\quad \bar{h}_j = \frac{h}{B_j}\,.$$

The 2nd derivatives of $\omega$ are discretized in the same way. The first derivatives of $\psi$ are approximated by:

$$(2.2.7)\qquad \begin{cases} A\dfrac{\partial\psi}{\partial\xi}\Big|_{i,j} \cong \dfrac{\psi_{i+1,j}-\psi_{i-1,j}}{2\bar{h}_i} \overset{\text{def}}{=\!=} -b_{i,j} \\[2ex] B\dfrac{\partial\psi}{\partial\eta}\Big|_{i,j} \cong \dfrac{\psi_{i,j+1}-\psi_{i,j-1}}{2\bar{h}_j} \overset{\text{def}}{=\!=} a_{i,j}\,. \end{cases}$$

The first derivatives of $\omega$ are discretized with Il'in's method (see Il'in [3]):

$$(2.2.8)\qquad \begin{cases} A\dfrac{\partial\omega}{\partial\xi}\Big|_{i,j} \cong \dfrac{(1+\alpha_{i,j})(\omega_{i+1,j}-\omega_{i,j}) + (1-\alpha_{i,j})(\omega_{i,j}-\omega_{i-1,j})}{2\bar{h}_i} \\[2ex] B\dfrac{\partial\omega}{\partial\eta}\Big|_{i,j} \cong \dfrac{(1+\beta_{i,j})(\omega_{i,j+1}-\omega_{i,j}) + (1-\beta_{i,j})(\omega_{i,j}-\omega_{i,j-1})}{2\bar{h}_j}\,, \end{cases}$$

with $\alpha_{i,j}$ and $\beta_{i,j}$ the Il'in coefficients:

$$(2.2.9)\quad \begin{cases} \alpha_{ij} = -\coth(\gamma_{i,j}a_{i,j}) + \dfrac{1}{\gamma_{i,j}a_{i,j}} \;;\; \gamma_{i,j} = \dfrac{\mathrm{Re}\,\max(h_{i-1},h_i)}{2}, \\ \\ \beta_{i,j} = -\coth(\delta_{i,j}b_{i,j}) + \dfrac{1}{\delta_{i,j}b_{i,j}} \;;\; \delta_{i,j} = \dfrac{\mathrm{Re}\,\max(h_{j-1},h_j)}{2}. \end{cases}$$

Because of this discretization artificial viscosity terms

$$(2.2.10)\quad -\frac{\alpha_{i,j}a_{i,j}\bar{h}_i}{2}\left(A^2\frac{\partial^2\omega}{\partial\xi^2}\right) \text{ and } -\frac{\beta_{i,j}b_{i,j}\bar{h}_j}{2}\left(B^2\frac{\partial\omega}{\partial\eta^2}\right)$$

are added in the right hand side of the vorticity equation of (2.1.2). The reason why Il'in discretization has been applied is as follows. Our multigrid method does not work if the matrix is not almost weakly diagonal dominant. This means that for Re >> 1 some form of artificial viscosity must be applied. In order to secure the existence of a Frechet derivative*) of the nonlinear system of discretized equations the artificial viscosity must be a smooth function of the coefficients. Il'in discretization serves this purpose; classical upwind differencing would not do.

The discretized NS-equations (2.1.2) are:

$$(2.2.11)\quad \begin{cases} p_{i,j}\psi_{i,j} + p_{i+1,j}\psi_{i+1,j} + p_{i-1,j}\psi_{i-1,j} + p_{i,j+1}\psi_{i,j+1} + \\ \qquad + p_{i,j-1}\psi_{i,j-1} + q_{i,j}\omega_{i,j} = 0 \\ \\ r_{i,j}\omega_{i,j} + r_{i+1,j}\omega_{i+1,j} + r_{i-1,j}\omega_{i-1,j} + r_{i,j+1}\omega_{i,j+1} + \\ \qquad + r_{i,j-1}\omega_{i,j-1} = 0 \end{cases}$$

with

---

*) For the Newton process, see section 2.3.

$$
(2.2.12)\qquad
\begin{cases}
p_{i,j} = \dfrac{1}{\bar{h}_i}\left(\dfrac{1}{h_{i-1}} + \dfrac{1}{h_i}\right) + \dfrac{1}{\bar{h}_j}\left(\dfrac{1}{h_{j-1}} + \dfrac{1}{h_j}\right) \\
p_{i-1,j} = \dfrac{-1}{\bar{h}_i h_{i-1}} \quad ; \quad p_{i+1,j} = \dfrac{-1}{\bar{h}_i h_i} \\
p_{i,j-1} = \dfrac{-1}{\bar{h}_j h_{j-1}} \quad ; \quad p_{i,j+1} = \dfrac{-1}{\bar{h}_j h_j} \\
q_{i,j} = M_{i,j} \\
r_{i,j} = \dfrac{p_{i,j}}{Re} - \dfrac{\alpha_{i,j} a_{i,j}}{\bar{h}_i} - \dfrac{\beta_{i,j} b_{i,j}}{\bar{h}_j} \\
r_{i-1,j} = \dfrac{p_{i-1,j}}{Re} - \dfrac{(1-\alpha_{i,j}) a_{i,j}}{2\bar{h}_i} \\
r_{i+1,j} = \dfrac{p_{i+1,j}}{Re} + \dfrac{(1+\alpha_{i,j}) a_{i,j}}{2\bar{h}_i} \\
r_{i,j-1} = \dfrac{p_{i,j-1}}{Re} - \dfrac{(1-\beta_{i,j}) b_{i,j}}{2\bar{h}_j} \\
r_{i,j+1} = \dfrac{p_{i,j+1}}{Re} + \dfrac{(1+\beta_{i,j}) b_{i,j}}{2\bar{h}_j} .
\end{cases}
$$

## 2.3. Linearization and simultaneous solution

The vorticity equation in (2.2.11) is non-linear. Methods to solve the non-linear NS equations can be classified in 3 groups:

1. Time-dependent methods. A time derivative is added and the problem is treated as an initial-value problem. As time becomes large, the desired state is approached (see ROACHE [8]).
2. Picard-iteration. These are methods generating a sequence of linear equations with constant coefficients. Each system of equations can be solved by a Fast Poisson Solver (see ROACHE [9] and [10]).
3. Newton-iteration. At each Newton step a linear system with variable coefficients has to be solved. Suitable iterative methods to solve such systems are the multigrid methods.

The last method offers good prospects. v. ASSELT [1] compares efficiencies of method 1 with those of method 3 applied to a Burgers-like equation with a small perturbation parameter. Method 3 appears to be most efficient

for this problem

Method 3 is also more efficient than method 2 when they are applied to the NS-equations with large Reynolds numbers (see WESSELING [13]).

Another property of (2.2.11) is that we have 2 equations with 2 unknowns (stream function and vorticity) in each point of the grid. In the methods 1 and 2 these equations are solved sequentially. When the problem has a no-slip boundary condition the time and Picard processes are very slow. Usually a relaxation parameter is added in the no-slip boundary condition, but it is difficult to get the optimal value of this parameter. Therefore, method 3 is applied with simultaneous solution of the streamfunction and vorticity equations.

Newton linearization of (2.2.11) gives:

$$
\begin{cases}
p_{i,j}\psi_{i,j} + p_{i+1,j}\psi^{\mu+1}_{i+1,j} + p_{i-1,j}\psi^{\mu+1}_{i-1,j} + p_{i,j+1}\psi^{\mu+1}_{i,j+1} \\
\qquad + p_{i,j-1}\psi^{\mu+1}_{i,j-1} + q_{i,j}\omega^{\mu+1}_{i,j} = 0 \\
r^{\mu}_{i,j}\omega^{\mu+1}_{i,j} + r^{\mu}_{i+1,j}\omega^{\mu+1}_{i+1,j} + r^{\mu}_{i-1,j}\omega^{\mu+1}_{i-1,j} + r^{\mu}_{i,j+1}\omega^{\mu+1}_{i,j+1} + \\
+ r^{\mu}_{i,j-1}\omega^{\mu+1}_{i,j-1} + s^{\mu}_{i,j}\psi^{\mu+1}_{i,j} + s^{\mu}_{i+1,j}\psi^{\mu+1}_{i+1,j} + s^{\mu}_{i-1,j}\psi^{\mu+1}_{i-1,j} + \\
\qquad + s^{\mu}_{i,j+1}\psi^{\mu+1}_{i,j+1} + s^{\mu}_{i,j-1}\psi^{\mu+1}_{i,j-1} = t^{\mu}_{i,j},
\end{cases}
\tag{2.3.1}
$$

with

$$
\begin{cases}
s^{\mu}_{i,j} = 0;\ s^{\mu}_{i+1,j} = -s^{\mu}_{i-1,j} = \dfrac{c^{\mu}_{i,j}}{2\bar{h}_i};\ s^{\mu}_{i,j+1} = -s^{\mu}_{i,j-1} = \dfrac{d^{\mu}_{i,j}}{2\bar{h}_j} \\
c^{\mu}_{i,j} = -\dfrac{(1+\beta^{\mu}_{i,j} + \beta'^{\mu}_{i,j}\delta_{i,j}b^{\mu}_{i,j})(\omega^{\mu}_{i,j+1} - \omega^{\mu}_{i,j})}{2\bar{h}_j} - \\
\qquad - \dfrac{(1-\beta^{\mu}_{i,j} - \beta'^{\mu}_{i,j}\delta_{i,j}b^{\mu}_{i,j})(\omega^{\mu}_{i,j} - \omega^{\mu}_{i,j-1})}{2\bar{h}_j}
\end{cases}
\tag{2.3.2}
$$

$$\begin{cases} d^{\mu}_{i,j} = \dfrac{(1+\alpha^{\mu}_{i,j} + \alpha'^{\mu}_{i,j}\gamma_{i,j}a^{\mu}_{i,j})(\omega^{\mu}_{i+1,j} - \omega^{\mu}_{i,j})}{2\bar{h}_i} + \\ \qquad + \dfrac{(1-\alpha^{\mu}_{i,j} - \alpha'^{\mu}_{i,j}\gamma_{i,j}a^{\mu}_{i,j})(\omega^{\mu}_{i,j} - \omega^{\mu}_{i-1,j})}{2\bar{h}_i} \\ t^{\mu}_{i,j} = a^{\mu}_{i,j}d^{\mu}_{i,j} - b^{\mu}_{i,j}c^{\mu}_{i,j}\,. \end{cases}$$

$a^{\mu}_{i,j}$ and $b^{\mu}_{i,j}$ are the velocities, $\alpha^{\mu}_{i,j}$ and $\beta^{\mu}_{i,j}$ the Il'in coefficients, $\alpha'^{\mu}_{i,j}$ and $\beta'^{\mu}_{i,j}$ the derivatives of the Il'in coefficients in the $\mu$th Newton step. For the derivation of (2.3.1) and (2.3.2) see appendix A.

## 2.4. The no-slip boundary condition

In many flow problems we encounter a no-slip boundary condition defined by:

$$(2.4.1) \qquad \begin{cases} \psi = 0 \\ \dfrac{\partial\psi}{\partial\xi} = 0 \end{cases} \qquad (\xi,\eta) \in \partial\Omega$$

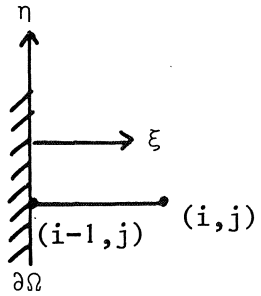


Figure 2.4.1.

Taylor expansion of $\psi$ in point (i,j) gives:

$$(2.4.2) \qquad \psi_{i,j} = \psi_{i-1,j} + h\left.\frac{\partial\psi}{\partial\xi}\right|_{i-1,j} + \frac{h^2}{2!}\left.\frac{\partial^2\psi}{\partial\xi^2}\right|_{i-1,j} + \frac{h^3}{3!}\left.\frac{\partial^3\psi}{\partial\xi^3}\right|_{i-1,j} + O(h^4).$$

$\psi_{i-1,j} = \left.\frac{\partial\psi}{\partial\xi}\right|_{i-1,j} = 0$ according to (2.4.1), while $\left.\frac{\partial^2\psi}{\partial\xi^2}\right|_{i-1,j} = \left(\frac{M\omega}{A^2}\right)_{i-1,j}$ according to the stream function equation in (2.1.2). The 3rd derivative of $\psi$ is equal to:

$$(2.4.3) \qquad \left.\frac{\partial^3\psi}{\partial\xi^3}\right|_{i-1,j} = \frac{\partial}{\partial\xi}\left.\left(\frac{\partial^2\psi}{\partial\xi^2}\right)\right|_{i-1,j} = \frac{\partial}{\partial\xi}\left(\frac{M\omega}{A^2}\right)_{i-1,j} =$$

$$= \frac{\left(\frac{M\omega}{A^2}\right)_{i,j} - \left(\frac{M\omega}{A^2}\right)_{i-1,j}}{h} + O(h)\,.$$

Therefore, (2.4.2) becomes:

$$\psi_{i,j} = \frac{h^2}{2}\left(\frac{M\omega}{A^2}\right)_{i-1,j} + \frac{h^2}{6}\left\{\left(\frac{M\omega}{A^2}\right)_{i,j} - \left(\frac{M\omega}{A^2}\right)_{i-1,j}\right\} + O(h^4) =$$

(2.4.4)

$$= \frac{\bar{h}_{i-1}^2}{3}(M\omega)_{i-1,j} + \frac{\bar{h}_i^2}{6}(M\omega)_{i,j} + O(h^4).$$

The vorticity in a point at the wall is approximated by:

$$\omega_{i-1,j} \cong \frac{1}{M_{i-1,j}}\left\{\frac{3}{\bar{h}_{i-1}^2}\psi_{i,j} - \frac{\bar{h}_i^2}{2\bar{h}_{i-1}^2}M_{i,j}\omega_{i,j}\right\}. \tag{2.4.5}$$

Substituting this boundary condition in the equations (2.3.1) gives:

$$\begin{cases} r_{i,j}^{\mu} := r_{i,j}^{\mu} - \dfrac{\bar{h}_i^2 M_{i,j}}{2\bar{h}_{i-1}^2 M_{i-1,j}} r_{i-1,j}^{\mu} \\ \\ s_{i,j}^{\mu} := \dfrac{3}{\bar{h}_{i-1}^2 M_{i-1,j}} r_{i-1,j}^{\mu} \end{cases} \tag{2.4.6}$$

## 2.5. Scaling of the equations

Equations (2.3.1) can be written in the following form:

$$Au = f, \tag{2.5.1}$$

with

$$\begin{cases} A = \begin{vmatrix} A_{11} & A_{12} \\ A_{21} & A_{22} \end{vmatrix}, \quad u = \begin{vmatrix} u_1 \\ u_2 \end{vmatrix} \quad f = \begin{vmatrix} f_1 \\ f_2 \end{vmatrix} \\ \\ A_{11} = \left| \cdots\cdots p_{i,j-1} \cdots\cdots p_{i-1,j} \quad p_{i,j} \quad p_{i+1,j} \cdots\cdots p_{i,j+1} \cdots \right| \\ A_{12} = \left| \cdots\cdots\cdots\cdots\cdots\cdots q_{i,j} \cdots\cdots\cdots\cdots\cdots\cdots \right| \end{cases} \tag{2.5.2}$$

$$\left\{\begin{array}{l} A_{21} = |\ldots s_{i,j-1}\cdots\cdots s_{i-1,j} \quad s_{i,j} \quad s_{i+1,j}\cdots\cdots s_{i,j+1}\cdots\cdots| \\ A_{22} = |\ldots r_{i,j-1}\cdots\cdots r_{i-1,j} \quad r_{i,j} \quad r_{i+1,j}\cdots\cdots r_{i,j+1}\cdots\cdots| \\ u_1 = |\psi_{i,j}| \quad ; \quad f_1 = |0| \\ u_2 = |\omega_{i,j}| \quad ; \quad f_2 = |t_{i,j}| \ . \end{array}\right.$$

The equations are scaled as follows. The rows of $A_{21}$ and $A_{22}$ are multiplicated with Re. The columns of $A_{12}$ and $A_{22}$ are multiplicated with a scaling factor $s_0$. Finally, all rows are multiplicated with a factor such that we have 4 in the maindiagonal of A.

The factor $s_0$ is chosen as follows:

$$(2.5.3) \qquad s_0 = h_0^2,$$

where $h_0$ is the smallest mesh size on the no-slip wall(s) in normal direction.

All coefficients of A are O(1) except

$$(2.5.4) \qquad q_{ij} = O\left(\frac{h_i^2 M_{i,j}}{s_0} \ , \quad \frac{h_j^2 M_{i,j}}{s_0}\right)$$

and $s_{i,j}$ in the no-slip boundary points:

$$(2.5.5) \qquad s_{i,j} = O\left(\frac{1}{M_{i,j}} \ , \ \frac{h_j}{h_i M_{i,j}} \ , \ \frac{h_j^2}{h_i^2 M_{i,j}}\right) \ .$$

Special cases are:

a) $M_{i,j} \to \infty$, $q_{i,j} \to \infty$ (e.g. large distances from a profile)

b) $M_{i,j} \to 0$, $s_{i,j} \to \infty$ (e.g. in the neighbourhood of a sharp trailing edge of a profile)

c) $h_0 \to 0$, $q_{i,j} \to \infty$ (strong stretching of coordinates at the no-slip boundary).

The submatrices $A_{11}$ and $A_{22}$ are diagonal dominant because of the Il'in

discretization (2.2.8). $A_{21}$ and $A_{22}$ may contain large coefficients, by which the system may be unstable. In chapter 6 and 7 we shall see that we can cope with this problem by cutting off the coefficients $q_{i,j}$ and $s_{i,j}$.

## 3. THE MULTIGRID METHOD FOR 2 VARIABLES

### 3.1. Multigrid operators

Let a set of grid functions $U^\ell$ corresponding to the grid $\Omega^\ell$ (2.2.1) be defined by:

$$(3.1.1) \qquad U^\ell = \{u^\ell : \{1(1)2\} \times \Omega^\ell \to \mathbb{R}\} .$$

System (2.5.1) is denoted now by:

$$(3.1.2) \qquad A^\ell u^\ell = f^\ell ,$$

with $A^\ell : U^\ell \to U^\ell$. The multigrid method uses a hierarchy of computational grids $\Omega^k$, $k = \ell-1(-1)1$:

$$(3.1.3) \qquad \Omega^k = \{(\xi_i,\eta_j) \mid \xi_i = (i2^{\ell-k}+1)h, \quad \eta_j = (j.2^{\ell-k}+1)h,$$

$$i = 0(1)2^k, \quad j = 0(1)2^k\}$$

(h is the mesh size of the finest grid $\Omega^\ell$), and corresponding sets of grid functions $U^k$, $k = \ell-1(-1)1$, defined by (3.1.1) with $\ell$ replaced by k. The mesh sizes of $\Omega^k$ are $2^{\ell-k}h$, hence the grids $\Omega^k$ are coarser as k gets smaller. Let us be given

$$\left.\begin{array}{ll} \text{restriction operators:} & R^k : U^k \to U^{k-1} \\ \text{prolongation operators:} & P^k : U^{k-1} \to U^k \\ \text{coarse grid operators:} & A^{k-1} : U^{k-1} \to U^{k-1} \\ \text{approximate inverses:} & B^k : U^k \to U^k \end{array}\right\} \quad k = 2(1)\ell$$

The multigrid program *MULGRI* can be described in quasi-Algol as follows:

(1) $r^{\ell} := f^{\ell} - A^{\ell}u^{\ell}$;
(2) for k := $\ell(-1)2$ do $r^{k-1} := R^k r^k$;
    $e^1 := (A^1)^{-1} r^1$;
    for k := $2(1)\ell$ do
(3) begin  $e^k := P^k e^{k-1}$;
(4)  $e^k := (I^k - B^k A^k)e^k + B^k r^k$;
    end
(5) $u^{\ell} := u^{\ell} + e^{\ell}$;

In order to describe the operators we use the same data structure as in MOL [5]. A set of ordered pairs $i = (i_1, i_2)$ is defined:

$$(3.1.4) \qquad N^k = \{i = (i_1, i_2) \in Z \mid i_{1,2} = 0(1)2^k\}, \quad Z = \mathbb{Z} \times \mathbb{Z}.$$

Furthermore, we define the set J:

$$(3.1.5) \qquad J = \{j = (j_1, j_2) \in Z \mid j_{1,2} = 0, \pm 1\}.$$

For $u^k \in U^k$ the value of the $\alpha$th unknown in point i will be denoted by $u^k_{\alpha i}$.

The matrix-vector multiplication is defined by:

$$(3.1.6) \qquad (A^k u^k)_{\alpha i} = \sum_{\beta=1}^{2} \sum_{j \in J} A^k_{\alpha\beta ij}\, u^k_{\beta, i+j} \qquad i \in N^k, \quad \alpha = 1,2.$$

The prolongation $P^k$ and the restriction $R^k$ are defined as follows:

$$(3.1.7) \qquad \begin{cases} (P^k u^{k-1})_{\alpha i} = 4 \sum_{j \in Z} t_{i-2j}\, u^{k-1}_{\alpha j}, & i \in N^k, \quad \alpha = 1,2. \\ (R^k u^k)_{\alpha i} = \sum_{j \in Z} t_j\, u^{k-1}_{\alpha, 2i+j}, & i \in N^{k-1}, \quad \alpha = 1,2. \end{cases}$$

$t_j$ is a 9-point weighting operator:

$$(3.1.8)\qquad t_j = \begin{cases} \frac{1}{4} & j = (0,0) \\ \frac{1}{8} & j = (1,0),\ (0,1),\ (-1,0),\ (0,-1) \\ \frac{1}{16} & j = (1,1),\ (-1,1),\ (-1,-1),\ (1,-1) \\ 0 & j \notin J\ . \end{cases}$$

The coarse grid operator $A^{k-1}$ is the Galerkin approximation $A^{k-1} = R^k A^k P^k$ and is computed as follows:

$$(3.1.9)\qquad A^{k-1}_{\alpha\beta ij} = 4 \sum_{\substack{u \\ u,v \in Z}} \sum_{v} t_u\ A^k_{\alpha\beta,2i+u,v+2j-u}\ t_v\ , \qquad \begin{array}{l} i \in N^{k-1},\ j \in J, \\ \alpha,\beta = 1,2. \end{array}$$

9p-APINV and 9p-ILU are used as smoothing operators*). The approximate inverse $B^k$ of the APINV-process is computed as follows:

$$(3.1.10)\qquad \begin{cases} \sum_{\beta=1}^{2} \sum_{j \in J} B^k_{\alpha\beta ij}\ A^k_{\beta,\gamma,i+j,s-j} = \delta^k_{\alpha\gamma 0s}\ , & i \in N^k,\ s \in J,\ \alpha,\gamma = 1,2. \\ B^k_{\alpha\beta ij} = 0\ , & i \in N^k,\ j \notin J,\ \alpha,\beta = 1,2. \end{cases}$$

$\delta$ is the Kronecker delta. The $L^k$ and $U^k$ for the ILU-process satisfy the relation:

$$(3.1.11)\qquad \sum_{\beta} \sum_{j} L^k_{\alpha\beta ij}\ U^k_{\beta\gamma,i+j,s-j} = A^k_{\alpha\gamma is}\ , \qquad i \in N^k,\ s \in J,\ \alpha,\gamma = 1,2.$$

The range of the indices j, $\beta$ and s-j at a given combination $\alpha,\gamma$ is defined in the following table.

---

* At the 2-variable problems, which are considered in this report, *MULGRI* with 9-point multigrid operators appear to be more efficient than *MULGRI* with 7-point multigrid operators. In MOL [5] it is shown that in several 1 variable cases the opposite is true.

| $\alpha$ | $\gamma$ | $\beta$ | j | s-j |
|---|---|---|---|---|
| 1 | 1 | 1 | $J^-$ | $J^+$ |
| 1 | 2 | 1 | $J^-$ | J |
| 2 | 1 | 1 | J | $J^+$ |
| 2 | 2 | 1,2 | $J,J^-$ | $J,J^+$ |

Table 3.1.1 Ranges of $\beta$, j, s-j at a given $\alpha,\gamma$

$J^+ = \{(0,0),(1,0),(-1,1),(0,1),(1,1)\}$

$J^- = \{(0,0),(-1,0),(1,-1),(0,-1),(-1,-1)\}$

$L^k$ and $U^k$ are constructed by a standard LU-decomposition algorithm writing zero outside a prescribed non-zero pattern. The rows of $A^k$, which correspond with points of the grid $\Omega^k$, are arranged in the order $(0,0),(1,0),(2,0),\ldots,(2^k,0),(0,1),(1,1),(2,1)\ldots\ldots,(2^k,1),\ldots\ldots(0,2^k),(1,2^k),\ldots\ldots(2^k,2^k)$. The construction of the 9p-ILU d-composition is illustrated in figure 3.1.1. The dots denote the places where ILU-corrections take place, the stars the places where the rest matrix $R^k = L^kU^k - A^k$ has elements $\neq 0$.

## 3.2. Computational complexity of one multigrid iteration

Consider the quasi-Algol program of *MULGRI* described in section 3.1. In step (1) we have to compute the residual on the finest grid. In MOL [5] is described how this can be done very efficiently by using the rest matrix. In examples with only 1 variable the rest matrix contains 2 diagonals for a 5-point $A^k$ and a 7p-ILU. In this 2 variables case the rest matrix contains many diagonals. It appears more efficient to compute $f^\ell - A^\ell u^\ell$ directly.

In table 3.2.1 the numbers of operations per point on a grid $\Omega^k$ for the different parts of program *MULGRI* are given. We assume that the sub-matrices $A^k_{11}$, $A^k_{21}$ and $A^k_{22}$ are 5-point matrices and $A^k_{12}$ a diagonal matrix corresponding to (2.5.2). As smoothing process 9p-ILU is used.

For the computation of the total number of operations on all levels some work is neglected: savings near the boundaries and the work on the coarsest grid. The coarse grid matrices $A^k_{ij}$, $k = \ell-1(-1)1$ are 9 point matrices. For convenience, we assume that these coarse grid matrices

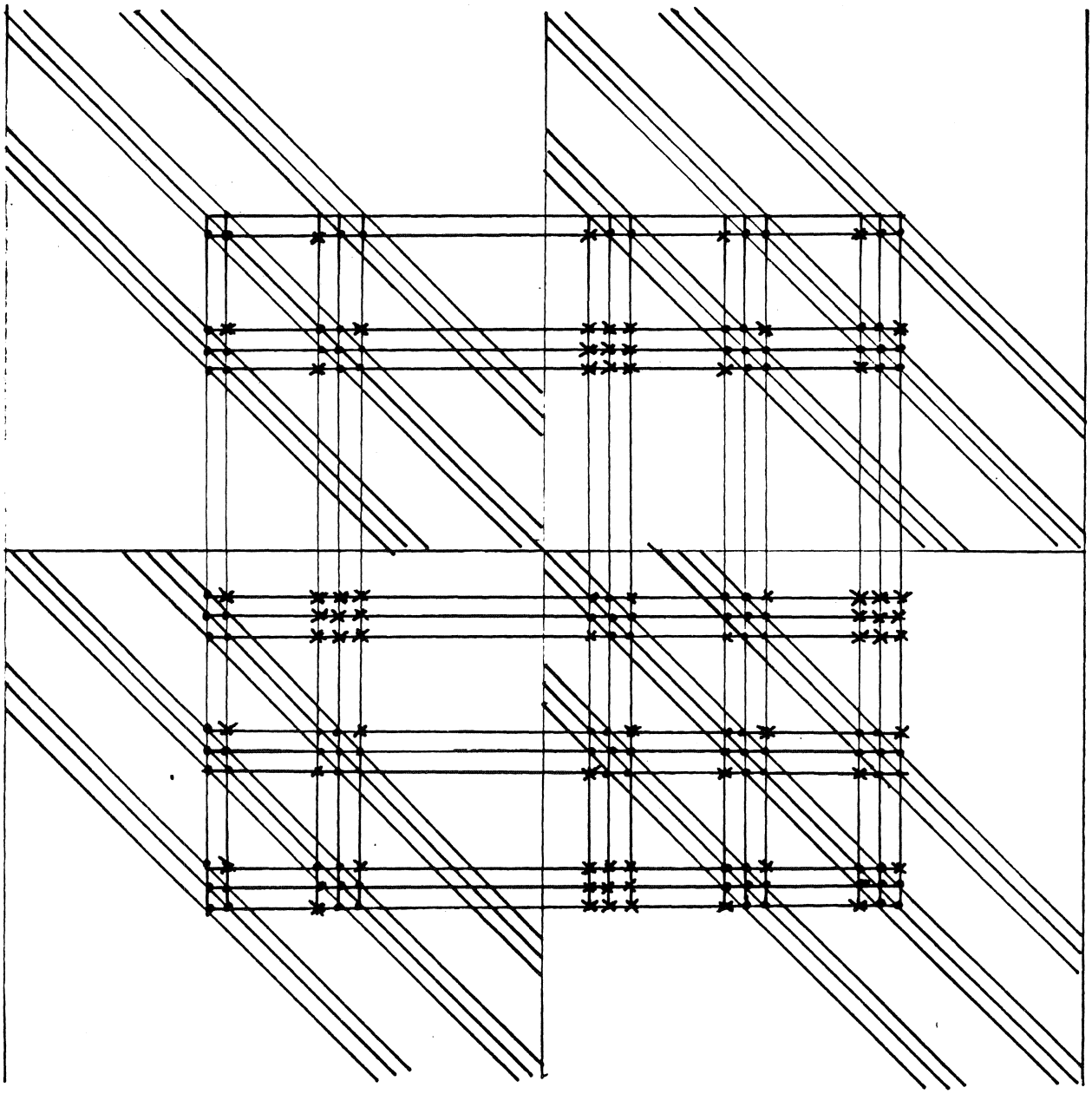

Figure 3.1.1 Computation of ILU-decomposition of $A^k$

| part of *MULGRI* | number of operations per point |
|---|---|
| $r^{k-1} := R^k r^k$ | 22 |
| $e^k := P^k e^{k-1}$ | 4 |
| $e^k := (I^k - B^k A^k) e^k + B^k r^k$ | 90 |
| $r^k := f^k - A^k u^k$<br>$u^k := u^k + e^k$ | 34 |

Table 3.2.1 Number of operations per point for the different parts of *MULGRI*

have the same point structure as the submatrices $A^{\ell}_{ij}$ on the finest grid.

Suppose the number of points on the finest grid is $N(=O(4^{\ell}))$. For $\ell$ large the total work W of one iteration with *MULGRI* is

| | | | |
|---|---|---|---|
| step (1) + step (5) | : | 34 N | operations |
| step (2) | : | $7\frac{1}{3}$ | " |
| step (3) | : | $5\frac{1}{3}$ | " |
| step (4) | : | 120 N | " |
| 1 iteration step | : | $W = 166\frac{2}{3}$ N | " |

The preliminary work before the multigrid process is:

| | | |
|---|---|---|
| computation $L^k, U^k$, $k = \ell(-1)2$ | : 252 N | operations. |
| computation $R^k A^k P^k$, $k = \ell(-1)2$ | : 328 N | " |

The total preliminary work is about 3.5 W.

## 4. THE SQUARE CAVITY FLOW

Consider the NS-equations (2.1.2) with:

(4.1) $A = B = M = 1,$

valid in the unit square with sizes H = 1.

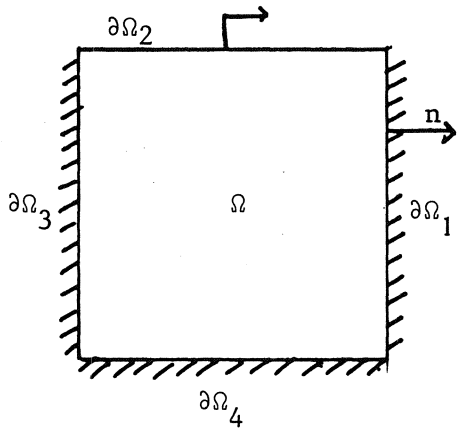


Figure 4.1. Square cavity

The boundary conditions are

$$\psi = 0, \quad \frac{\partial\psi}{\partial n} = g, \tag{4.2}$$

with $g = 0$ on $\partial\Omega_1$, $\partial\Omega_3$, $\partial\Omega_4$ and $g = 1$ on $\partial\Omega_2$.

The multigrid iterations are terminated when the maximum of the difference between two iterands is smaller than $10^{-6}$

$$|(u^{\ell})^{(\nu+1)} - (u^{\ell})^{(\nu)}| < 10^{-6}. \tag{4.3}$$

Furthermore, the average reduction factor is defined:

$$r_{av} = \left(\frac{|(u^{\ell})^{(\nu_0+1)} - (u^{\ell})^{(\nu_0)}|}{|(u^{\ell})^{(1)} - (u^{\ell})^{(0)}|}\right)^{1/\nu_0}, \quad \nu_0 \neq 0, \tag{4.4}$$

with $\nu_0$ the smallest integer such that (4.3) holds. The Newton iterations are terminated if

$$|(u^{\ell})^{(\mu+1)} - (u^{\ell})^{(\mu)}| < 10^{-4}. \tag{4.5}$$

Experiments have been made for Reynolds numbers Re = 10,50,150. At

Re = 10 we start with the zero solution, at the other Reynolds numbers with the solution of the preceding lower Reynolds numbers. Table 4.1 gives the results for *MULGRI* with APINV and table 4.2 for *MULGRI* with ILU as smoothing operator.

| Re | h | $\nu_0^{(1)}$ | $\nu_0^{(2)}$ | $\nu_0^{(3)}$ | $r_{av}^{(1)}$ | $r_{av}^{(2)}$ | $r_{av}^{(3)}$ |
|---|---|---|---|---|---|---|---|
| 10 | 1/6 | 7 | 4 | | 0.14 | 0.15 | |
| | 1/10 | 12 | 5 | | 0.32 | 0.27 | |
| | 1/18 | 13 | 5 | | 0.35 | 0.26 | |
| | 1/34 | 13 | 5 | | 0.36 | 0.25 | |
| 50 | 1/6 | 9 | 7 | 2 | 0.19 | 0.20 | 0.18 |
| | 1/10 | 14 | 10 | 3 | 0.35 | 0.32 | 0.23 |
| | 1/18 | 16 | 11 | 3 | 0.39 | 0.36 | 0.30 |
| | 1/34 | 16 | 11 | 3 | 0.39 | 0.34 | 0.20 |
| 150 | 1/6 | 11 | 9 | 4 | 0.28 | 0.23 | 0.22 |
| | 1/10 | 15 | 12 | 6 | 0.37 | 0.38 | 0.36 |
| | 1/18 | 15 | 13 | 5 | 0.37 | 0.40 | 0.30 |
| | 1/34 | 16 | 13 | 4 | 0.38 | 0.39 | 0.26 |

Table 4.1. Results *MULGRI* (with APINV) applied to the square cavity flow

$\nu_0^{(\mu)}$: number of multigrid iterations in $\mu$th Newton step

$r_{av}^{(\mu)}$: average reduction factor in $\mu$th Newton step

| Re | h | $\nu_0^{(1)}$ | $\nu_0^{(2)}$ | $\nu_0^{(3)}$ | $r_{av}^{(1)}$ | $r_{av}^{(2)}$ | $r_{av}^{(3)}$ |
|---|---|---|---|---|---|---|---|
| 10 | 1/6 | 4 | 2 | | 0.027 | 0.026 | |
| | 1/10 | 5 | 2 | | 0.059 | 0.033 | |
| | 1/18 | 5 | 2 | | 0.056 | 0.034 | |
| | 1/34 | 5 | 2 | | 0.056 | 0.034 | |
| 50 | 1/6 | 5 | 4 | 2 | 0.031 | 0.042 | 0.049 |
| | 1/10 | 5 | 4 | 1 | 0.052 | 0.061 | 0.056 |
| | 1/18 | 6 | 4 | 2 | 0.082 | 0.056 | 0.051 |
| | 1/34 | 6 | 4 | 2 | 0.083 | 0.062 | 0.052 |
| 150 | 1/6 | 7 | 6 | 3 | 0.099 | 0.092 | 0.079 |
| | 1/10 | 6 | 5 | 3 | 0.083 | 0.084 | 0.078 |
| | 1/18 | 6 | 5 | 3 | 0.080 | 0.083 | 0.064 |
| | 1/34 | 6 | 5 | 2 | 0.081 | 0.082 | 0.063 |

Table 4.2. Results *MULGRI* (with ILU) applied to the square cavity flow. For legenda see table 4.1.

Note that *MULGRI* with ILU is about 2 times faster than *MULGRI* with APINV. Because the computational complexity of 1 APINV step is larger than the complexity of 1 ILU step, *MULGRI* with ILU is more efficient. From now on, we apply only the last method.

We remark that the number of multigrid iterations does not increase as $h \downarrow 0$ and is insensitive to changes induced by Newton iteration.

Furthermore, the number of multigrid iterations is comparible with that of the Poisson equation (4 iterations at mesh size h = 1/18 and the same termination criterium).

At large Reynolds numbers the multigrid process diverges. The reason is that as $Re \to \infty$ the discretization at the walls becomes so skew that the boundary conditions do not have influence. Therefore, mesh refinement is necessary in the boundary layers. This is not applied here because the square cavity problem is only a test problem and does not have physical importance.

## 5. THE FLOW AROUND A CYLINDER

We consider the steady 2D flow of an incompressible viscous flow about a circular cylinder. The origin is at the centre of the circular cross-section of the cylinder with positive x-axis in the direction of the incident uniform flow at infinity. The radius R of the cylinder and the speed V of the free stream flow are used as the units of length and speed respectively, to introduce dimensionless variables. The non-dimensional situation is given in figure 5.1, where the flow field is bounded by a large circle with radius $e^{\pi} \cong 23.14$.

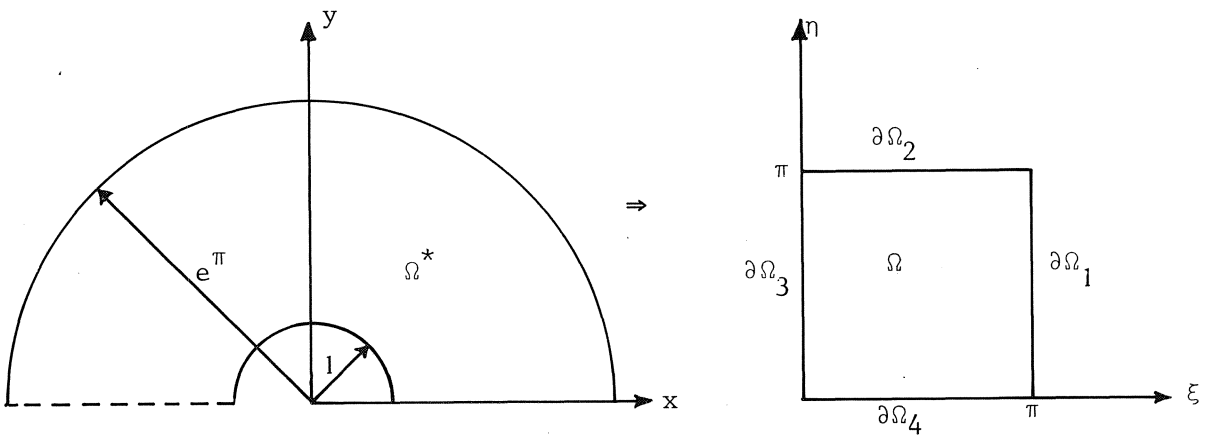


Figure 5.1. Flow region cylinder mapped on a square.

This flow field is mapped by the inverse transformation of

$$(5.1) \qquad x = e^{\xi}\cos\eta, \qquad y = e^{\xi}\sin\eta,$$

on a square $\Omega$ with size $H = \pi$ in the $(\xi,\eta)$-plane. The transformed NS-equations are (2.1.2) with

$$(5.2) \qquad A = B = 1, \qquad M = e^{2\xi}.$$

The Reynolds number is defined by

$$(5.3) \qquad Re = \frac{VR}{\nu},$$

where $\nu$ is the coefficient of kinematic viscosity of the fluid.

The grid $\Omega^{\ell}$ (2.2.1) in the $(\xi,\eta)$-plane has uniform mesh size. The corresponding grid in the (x,y)-plane has uniform mesh size in angular direction and in radial direction a mesh size which is small in the neighbourhood of the cylinder and is growing larger away from the cylinder.

The boundary conditions are:

$$(5.4)\qquad \begin{cases} \psi = \dfrac{\partial \psi}{\partial \xi} = 0 & (\xi,\eta) \in \partial\Omega_3 \\ \omega = \psi = 0 & (\xi,\eta) \in \partial\Omega_2,\ \partial\Omega_4 \\ \omega = 0,\ \psi = e^{\xi}\sin\eta & (\xi,\eta) \in \partial\Omega_1. \end{cases}$$

The same termination criteria are used as in the square cavity case. The results with *MULGRI* (with ILU) are presented in table 5.1.

| Re | h | $\nu_0^{(1)}$ | $\nu_0^{(2)}$ | $\nu_0^{(3)}$ | $r_{av}^{(1)}$ | $r_{av}^{(1)}$ | $r_{av}^{(2)}$ |
|---|---|---|---|---|---|---|---|
| 10 | $\pi/6$ | 7 | 5 | 1 | 0.140 | 0.110 | 0.034 |
| | $\pi/10$ | 7 | 5 | 1 | 0.139 | 0.120 | 0.053 |
| | $\pi/18$ | 7 | 5 | 1 | 0.141 | 0.119 | 0.064 |
| | $\pi/34$ | 8 | 5 | 1 | 0.170 | 0.100 | 0.029 |
| 50 | $\pi/6$ | 8 | 5 | 1 | 0.178 | 0.106 | 0.042 |
| | $\pi/10$ | 8 | 6 | 2 | 0.180 | 0.150 | 0.063 |
| | $\pi/18$ | 8 | 6 | 3 | 0.175 | 0.153 | 0.068 |
| | $\pi/34$ | 8 | 6 | 3 | 0.185 | 0.154 | 0.092 |
| 150 | $\pi/6$ | 8 | 7 | 4 | 0.180 | 0.201 | 0.105 |
| | $\pi/10$ | 8 | 6 | 4 | 0.185 | 0.160 | 0.105 |
| | $\pi/18$ | 8 | 7 | 4 | 0.186 | 0.200 | 0.108 |
| | $\pi/34$ | 8 | 7 | 4 | 0.187 | 0.195 | 0.110 |

Table 5.1. Results *MULGRI* applied to the flow around a cylinder. For legenda see table 4.1.

The average reduction factors are greater than in the square cavity case, but they are still insensitive to h and to changes in the coefficients

induced by Newton iteration. A reason for the slower convergence of *MULGRI* is due to the big coefficients $q_{i,j}$ in the coefficient matrix ($1 \leq M_{i,j} < 536$ in the points $(\xi_i, \eta_i) \in \Omega^{\ell} \cup \partial\Omega^{\ell}$). In order to test the solutions obtained by *MULGRI* applied on this cylinder problem, we compute some specific quantities at some Reynolds numbers and compare these results with those of other authors. The friction drag coefficient $C_p$ and the pressure drag coefficient $C_f$ are defined as follows:

$$(5.5) \qquad \begin{cases} C_f = \dfrac{2}{Re} \displaystyle\int_0^{\pi} \omega \sin\eta \, d\eta \\ \\ C_p = \dfrac{-2}{Re} \displaystyle\int_0^{\pi} \dfrac{\partial\omega}{\partial\xi} \sin\eta \, d\xi \end{cases}$$

The pressure in the leading edge of the cylinder is:

$$(5.6) \qquad p(\pi) = -\int_0^{\pi} \left(\frac{1}{Re}\frac{\partial\omega}{\partial\eta} - u\frac{\partial u}{\partial\xi}\right)d\xi, \qquad u = \frac{-1}{e^{\xi}}\frac{\partial\psi}{\partial\eta}$$

and in the trailing edge of the cylinder:

$$(5.7) \qquad p(0) = p(\pi) + \int_0^{\pi} \frac{1}{Re}\frac{\partial\omega}{\partial\xi}\, d\xi$$

For the derivation of these quantities see appendix B. In table 5.2 the quantities are presented for several Re-numbers and compared with results of other authors.

## 6. THE SYMMETRIC FLOW AROUND A KARMAN-TREFFTZ PROFILE

We consider the 2D-flow around a Karman-Trefftz profile with thickness $\varepsilon$, a trailing edge angle $(2-k)\pi$, camber $\gamma$ and length $2\ell$. The angle of incidence of the free stream flow is zero. The flow field in the upper half plane and bounded by a contour is mapped on the region around a cylinder, which we considered in the preceding chapter. The last region is mapped on a square with size $H = \pi$.

| Source of data | Reynolds number | | | | | | | |
|---|---|---|---|---|---|---|---|---|
| | 1 | 5 | 7 | 10 | 20 | 40 | 70 | 100 |
| | Friktion drag coefficient $C_f$ | | | | | | | |
| MO | 6.382 | 1.982 | 1.562 | 1.208 | 0.743 | 0.489 | 0.335 | 0.265 |
| DC | - | 1.917 | 1.553 | 1.246 | 0.812 | 0.524 | 0.360 | 0.282 |
| TK | - | - | - | - | - | - | - | - |
| TO | 6.941 | 2.183 | 1.757 | 1.402 | 0.903 | 0.580 | 0.405 | 0.322 |
| | Pressure drag coefficient $C_p$ | | | | | | | |
| MO | 6.482 | 2.255 | 1.861 | 1.527 | 1.136 | 1.028 | 0.880 | 0.710 |
| DC | - | 2.199 | 1.868 | 1.600 | 1.233 | 0.998 | 0.852 | 0.774 |
| TK | - | - | - | - | - | - | - | - |
| TO | 7.072 | 2.478 | 2.092 | 1.775 | 1.350 | 1.095 | 0.956 | 0.882 |
| | Drag coefficient $C_d = C_f + C_p$ | | | | | | | |
| MO | 12.869 | 4.236 | 3.423 | 2.735 | 1.879 | 1.517 | 1.215 | 0.975 |
| DC | - | 4.116 | 3.421 | 2.846 | 2.045 | 1.522 | 1.212 | 1.056 |
| TK | 10.109 | - | 3.303 | 2.800 | 2.013 | 1.536 | - | - |
| TO | 14.013 | 4.661 | 3.849 | 3.177 | 2.253 | 1.675 | 1.361 | 1.204 |
| | Pressure leading edge $p(\pi)$ | | | | | | | |
| MO | 4.536 | 1.897 | 1.667 | 1.483 | 1.223 | 1.107 | 1.065 | 1.047 |
| DC | - | 1.872 | 1.660 | 1.489 | 1.269 | 1.144 | 1.085 | 1.060 |
| TK | 3.905 | - | 1.637 | 1.474 | 1.261 | 1.141 | - | - |
| TO | 5.501 | 2.225 | 1.959 | 1.744 | 1.457 | 1.312 | 1.269 | 1.255 |
| | Pressure trailing edge $p(0)$ | | | | | | | |
| MO | 3.732 | 1.111 | 0.885 | 0.713 | 0.570 | 0.498 | 0.420 | 0.390 |
| DC | - | 1.044 | 0.870 | 0.742 | 0.589 | 0.509 | 0.439 | 0.393 |
| TK | 2.719 | - | 0.783 | 0.670 | 0.537 | 0.512 | - | - |
| TO | 3.547 | 1.081 | 0.906 | 0.773 | 0.614 | 0.543 | 0.493 | 0.453 |

Table 5.2. Comparison with other authors

MO: results with *MULGRI* (with $h = \pi/18$), DC: DENNIS and CHANG [2]

TK: TAKAMI and KELLER [11], TO: TUANN and OLSON [12].

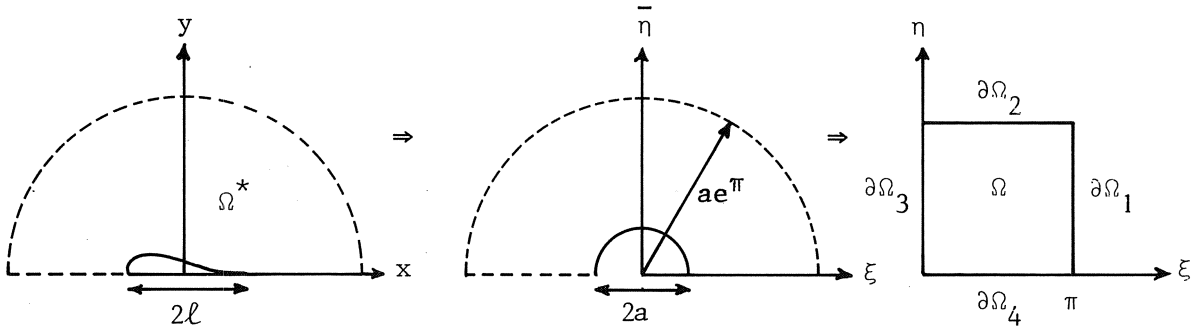


Figure 6.1. Flow region Karman-Trefftz profile mapped on a square.

The (conform) transformations of the regions are as follows. From $(\xi,\eta)$ to the $(\bar\xi,\bar\eta)$ plane:

$$(6.1)\qquad \begin{cases} \bar\xi = ae^{\xi}\cos\eta \\ \\ \bar\eta = ae^{\xi}\sin\eta \end{cases}$$

and from $(\bar\xi,\bar\eta)$-plane to the (x,y)-plane:

$$(6.2)\qquad z = f(\bar\zeta) \qquad\qquad z = x + iy, \quad \bar\zeta = \bar\xi + i\bar\eta$$

with

$$(6.3)\qquad \begin{cases} a = \dfrac{2\ell(\varepsilon + \sqrt{1-\gamma^2})^{k-1}}{(2\sqrt{1-\gamma^2})^{k}} \\ \\ f(\bar\zeta) = \dfrac{(\bar\zeta-\bar\zeta_T)^{k}}{\{\bar\zeta-\bar\zeta_T+a(\sqrt{1-\gamma^2}-\varepsilon)\}^{k-1}} + \ell \\ \\ \bar\zeta_T = a(\sqrt{1-\gamma^2}-i\gamma)\ . \end{cases}$$

Our choice for the parameters of the profile is:

(6.4) $\varepsilon = 0.05, \quad k = 1.99, \quad \gamma = 0, \quad \ell = 2.$

The transformed NS-equations are (2.1.2) with

(6.5) $A = B = 1, \quad M = a^2 |f'(\bar{\zeta})|^2 e^{2\xi}$ .

The boundary conditions are (5.4). The termination criteria for the Newton and multigrid processes are the same as in the square cavity case.

| Re | h | $\nu_0^{(1)}$ | $\nu_0^{(2)}$ | $\nu_0^{(3)}$ | $r_{av}^{(1)}$ | $r_{av}^{(2)}$ | $r_{av}^{(3)}$ |
|---|---|---|---|---|---|---|---|
| 10 | $\pi/6$ | 6 | 5 | 3 | 0.120 | 0.096 | 0.070 |
| | $\pi/10$ | 6 | 6 | 3 | 0.128 | 0.126 | 0.092 |
| | $\pi/18$ | 6 | 5 | 3 | 0.130 | 0.115 | 0.091 |
| 50 | $\pi/6$ | 6 | 5 | 3 | 0.137 | 0.142 | 0.126 |
| | $\pi/10$ | 6 | 4 | 2 | 0.176 | 0.148 | 0.134 |
| | $\pi/18$ | 6 | 4 | 2 | 0.143 | 0.138 | 0.133 |

Table 6.1. Results *MULGRI* applied to the flow around a Karman-Trefftz profile. For legenda see table 4.1.

For mesh size $h = \pi/18$ ($\ell = 3$) we have to cut off the coefficients $q_{i,j}$ in the coefficient matrix $A^\ell$ in the points where we can expect that the vorticity is zero:

(6.6) $q_{i,j} := c_0 \cdot q_{i,j} \qquad i \geq 2^{\ell-1} \wedge j \geq 2^{\ell-1}$ ,

with $c_0$ a coefficient such that the resulting $q_{ij} = 0(10)$. When this cutting is omitted, *MULGRI* diverges, probably because the coefficients $q_{i,j}$ and $s_{i,j}$ are too large with regard to the other coefficients in the matrix $A^\ell$. (See (2.5.4) and (2.5.5) and the fact that $|f'(\bar{\zeta})| = 0$ in the trailing edge, $|f'(\bar{\zeta})| = 1$ at infinity, $a = 1.0568$ therefore $0 < M_{i,j} < 600$ in the gridpoints $(\xi_i, \eta_j) \in \Omega^\ell \cup \partial\Omega^\ell$).

From table 6.1 it can be concluded that the numbers of multigrid itera-

tions are smaller than in the cylinder case and they are insensitive to h and changes in the coefficients induced by Newton iteration.

In figure 6.2 and 6.3 the vorticity (multiplicated with 100) for Re = 50 and h = $\pi/10$ is given around the Karman-Trefftz profile. We distinguish a boundary layer and a wake. These are the regions where $|\omega_{i,j}| > 0.5.10^{-2}$. The physical boundary layer has a thickness $O(1/\sqrt{Re})$ and the physical wake an angle $O(1/\sqrt{Re})$. In point i = 2, j = 4 of the grid $\Omega^{\ell}$ the boundary layer is about $16/\sqrt{Re}$ and in the point i = 8, j = 1 the wake angle is about $4/\sqrt{Re}$. So the physical boundary layer is not well represented.

In the figures 6.4 and 6.5 we look at the order of magnitude of the following quantities:

$$(6.7) \qquad c_{\xi} = \frac{\left|\frac{\alpha_{i,j} a_{i,j} \bar{h}_i}{2} A^2 \frac{\partial^2 \omega}{\partial \xi^2}\right|}{\left|\frac{1}{Re}\{A\frac{\partial}{\partial \xi}(A\frac{\partial \omega}{\partial \xi})\}\right|} \text{ and } c_{\eta} = \frac{\left|\frac{\beta_{i,j} b_{i,j} \bar{h}_j}{2} B^2 \frac{\partial^2 \omega}{\partial \eta^2}\right|}{\left|\frac{1}{Re}\{B\frac{\partial}{\partial \eta}(B\frac{\partial \omega}{\partial \eta})\}\right|}.$$

These quantities are only defined in the boundary layer and the wake. They represent the ratio of the artificial viscosity terms (2.2.10) induced by the Il'in upwind discretization and the viscosity terms in the NS equations (2.1.2). In the region with vorticity is zero, it doesn't matter how large the artificial viscosities

$$\frac{\alpha_{i,j} a_{i,j} \bar{h}_i}{2} \quad \text{and} \quad \frac{\beta_{i,j} b_{i,j} \bar{h}_j}{2}$$

are. From the figures it can be concluded that we have to choose smaller mesh sizes $\bar{h}_i$ and $\bar{h}_j$ in the boundary layer and the wake.

In figure 6.6 the vorticity on the profile is given for Re = 50 and h = $\pi/18$.

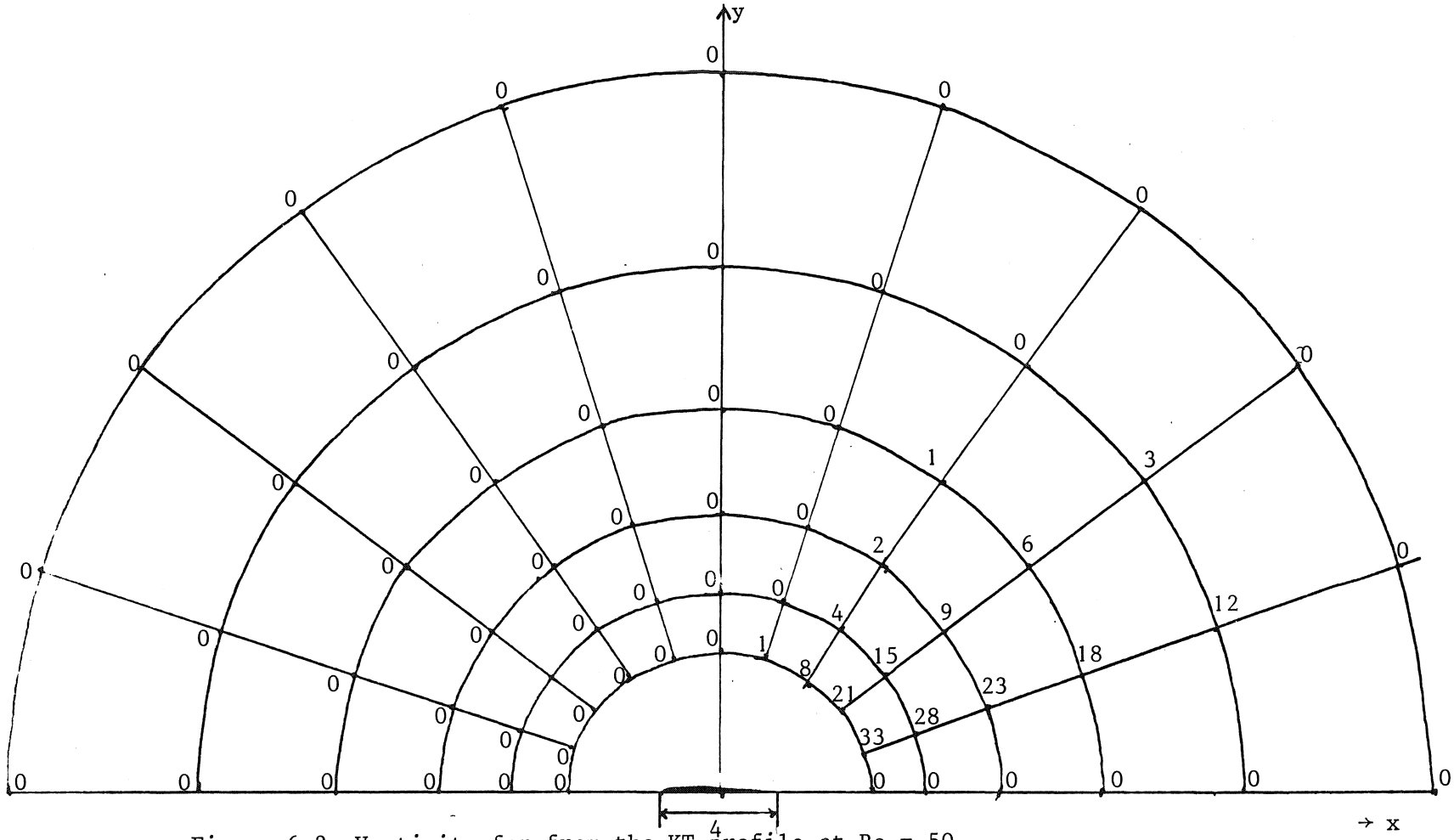


Figure 6.2. Vorticity far from the KT profile at Re = 50.

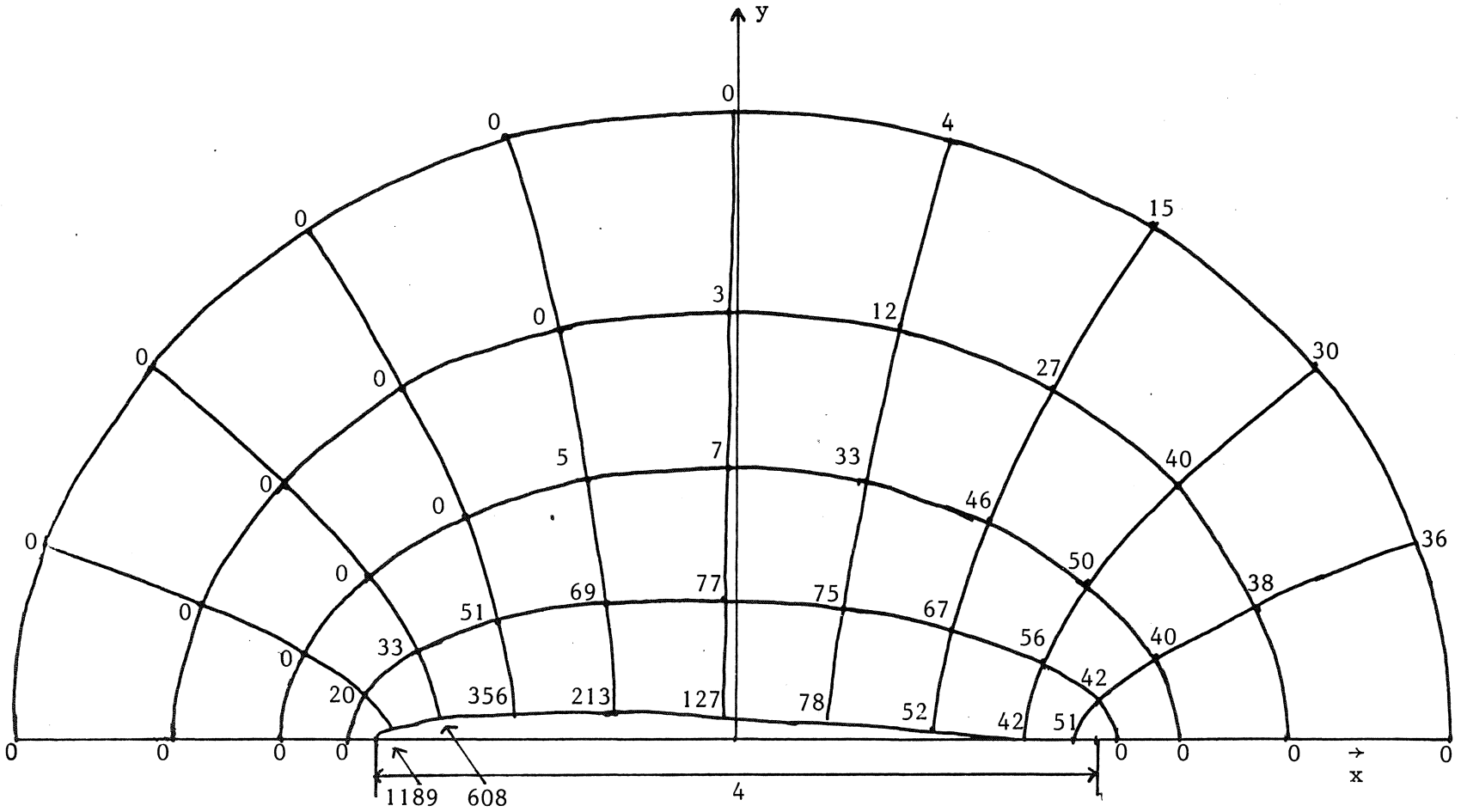


Figure 6.3. Vorticity in the neighbourhood of the KT profile at Re = 50

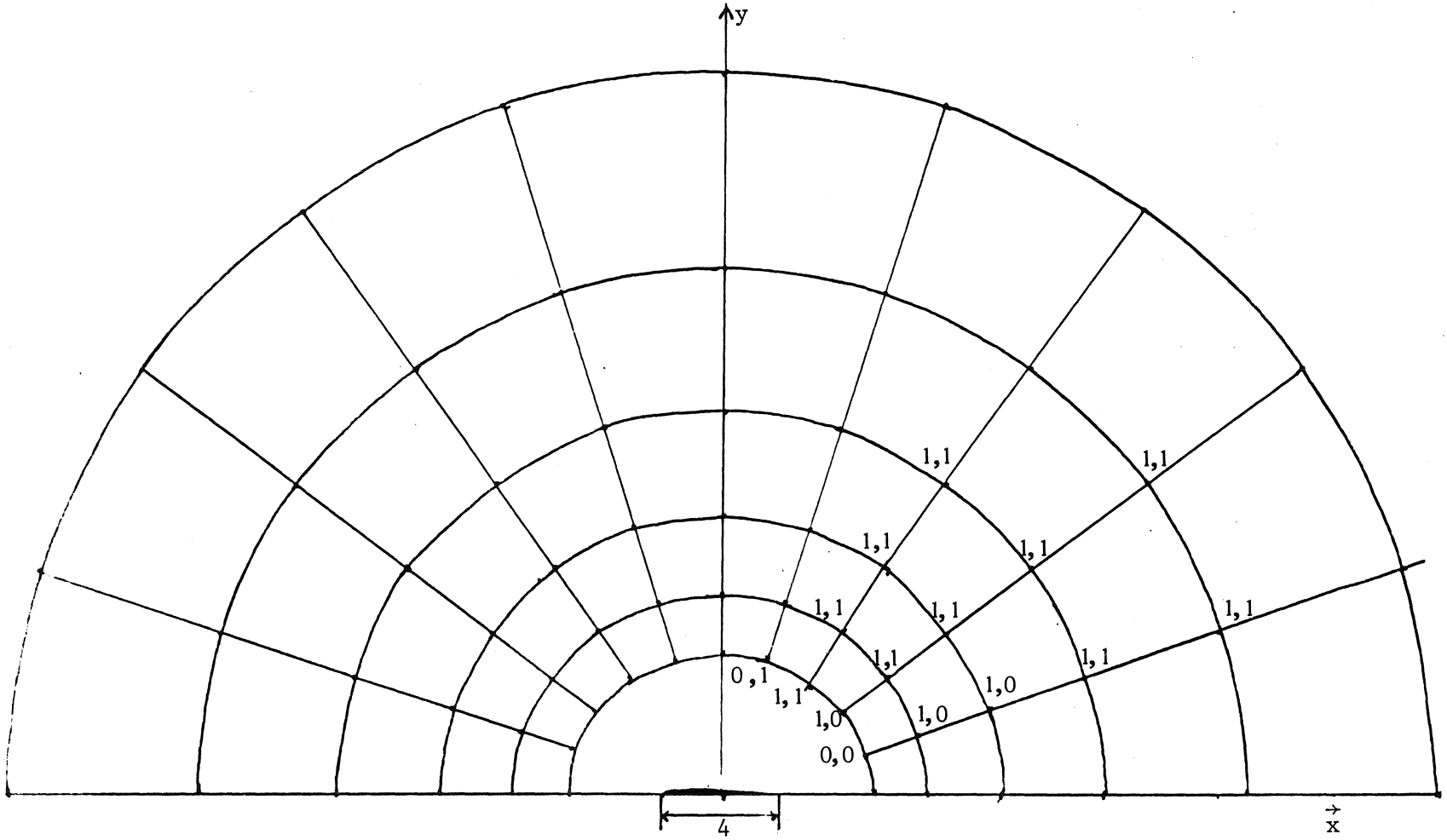


Figure 6.4. Order of magnitude of $c_\xi$ and $c_\eta$ defined in (6.7) at Re = 50. Before and after the comma $O(c_\xi)$ and $O(c_\eta)$ respectively with $O(c_\xi)$ = entier (log $c_\xi$) and $O(c_\eta)$ = entier (log $c_\eta$).

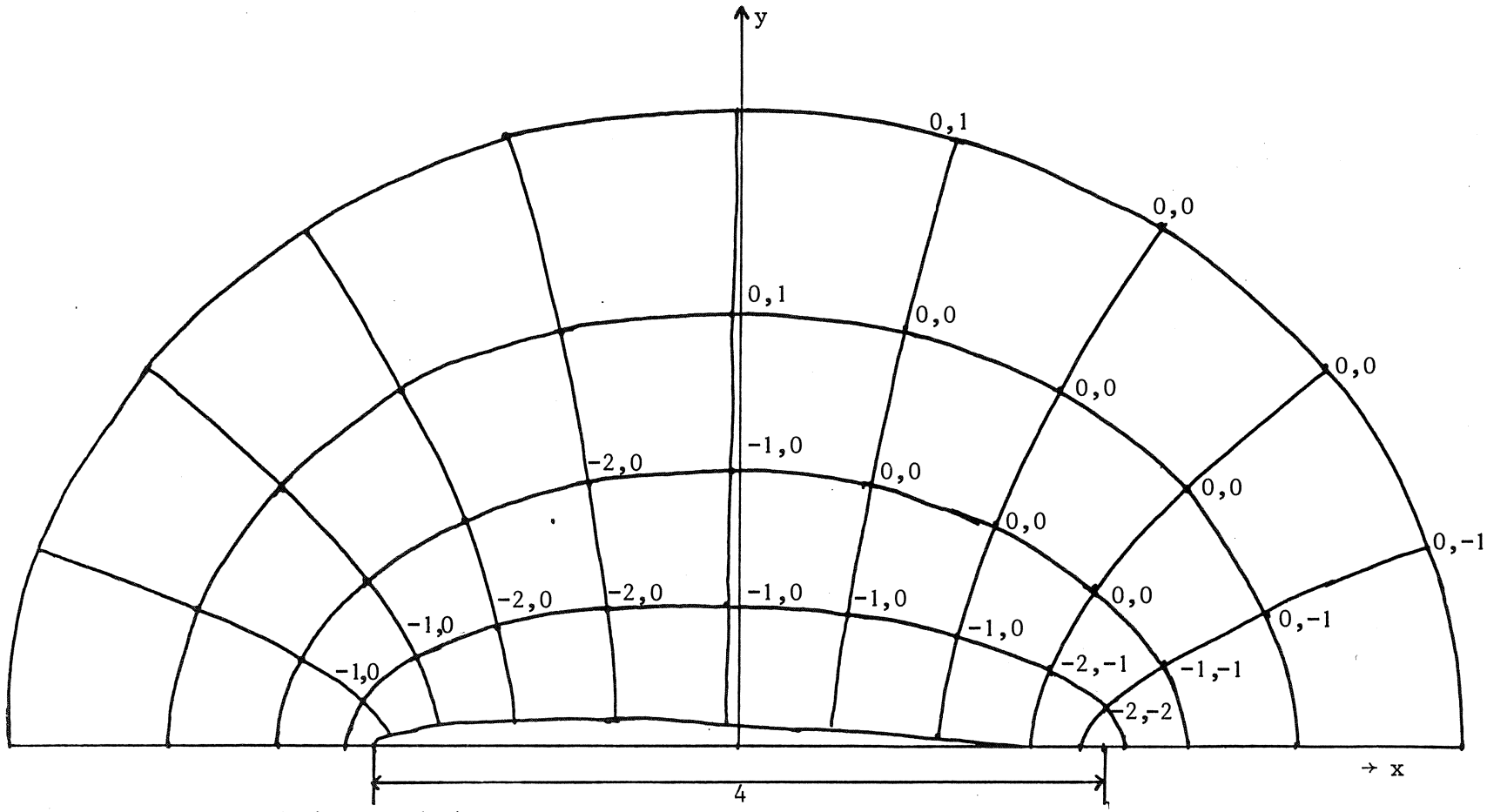


Figure 6.5. $O(c_\xi)$ and $O(c_\eta)$ at Re = 50
For legenda see figure 6.4.

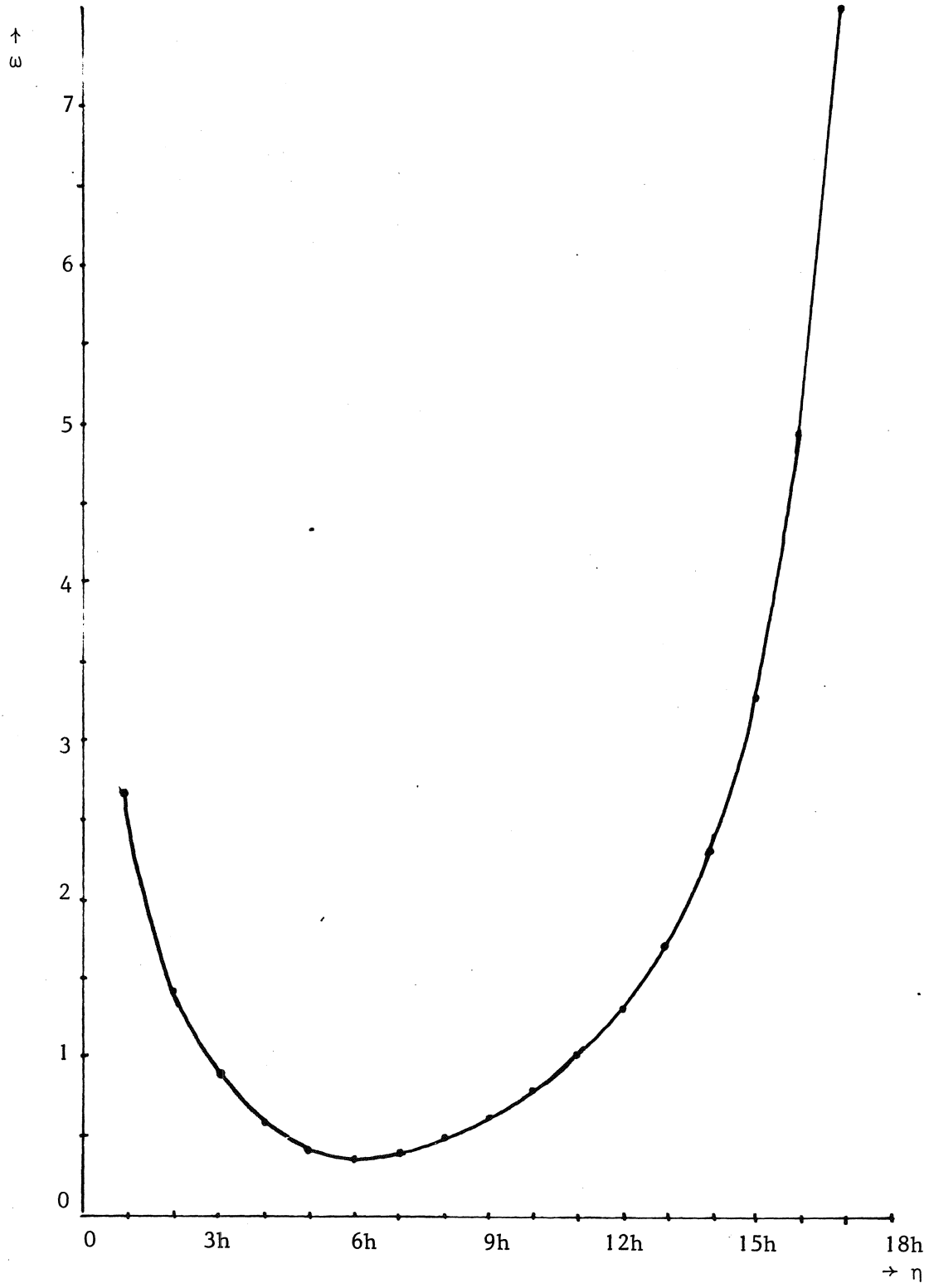


Figure 6.6. Vorticity on KT profile at Re = 50 ($h = \frac{\pi}{18}$)

## 7. MESH REFINEMENT

In the preceding section we have seen that mesh refinement is necessary in the boundary layer and in the wake. The following stretching functions are chosen:

$$(7.1)\qquad \begin{cases} \xi = c_0\{\xi' + c_1 \tanh(\frac{3\xi'}{\xi'_{bo}})\} \\ \eta = d_0\{\eta' + d_1 \tanh(\frac{3\eta'}{\eta'_{bo}})\} \end{cases}$$

with constants $c_0$, $d_0$, $c_1$ and $d_1$:

$$(7.2)\qquad \begin{cases} c_1 = V_1(\pi - \xi'_{bo}) - \xi'_{bo} \ ; & c_0 = \dfrac{\pi}{\pi + c_1 \tanh(\frac{3\pi}{\xi'_{bo}})} \\ d_1 = V_2(\pi - \eta'_{bo}) - \eta'_{bo} \ ; & d_0 = \dfrac{\pi}{\pi + d_1 \tanh(\frac{3\pi}{\eta'_{bo}})} \end{cases}.$$

$\xi'_{bo}$ and $\eta'_{bo}$ are bounds of the numerical boundary layer and the numerical wake respectively. $V_1$ is the ratio of coordinate lines inside/outside the boundary layer and $V_2$ the same ratio for the wake.

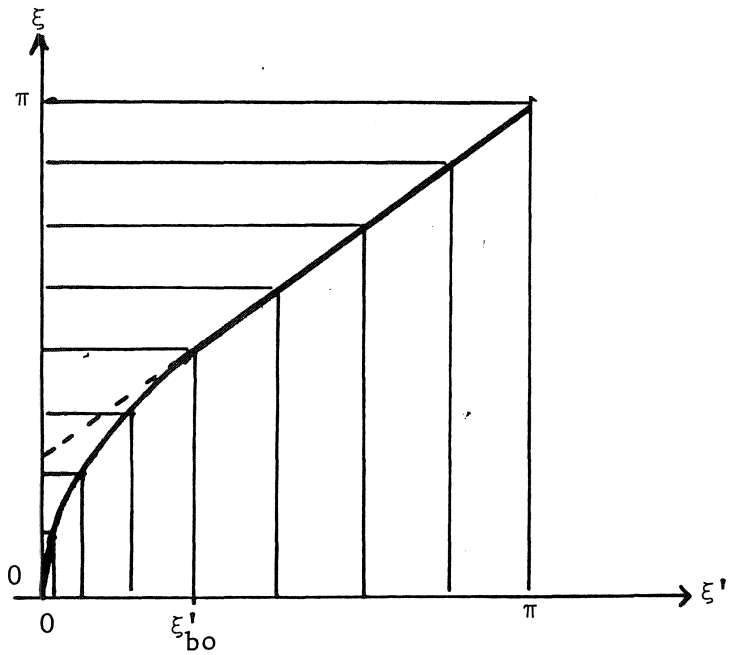


Figure 7.1. Stretching function $\xi = \xi(\xi')$ with $V_1 = \xi'_{bo} = 1$.

The mesh size is equidistant outside the numerical boundary layer. At no-slip boundaries the coefficients $s^{\mu}_{ij}$ (2.4.6) may be large because $\bar{h}_{i-1} = \frac{h}{A_{i-1}}$ is small. Therefore we choose:

(7.3) $$\bar{h}_{i-1} = \bar{h}_i$$

at the no-slip boundary.

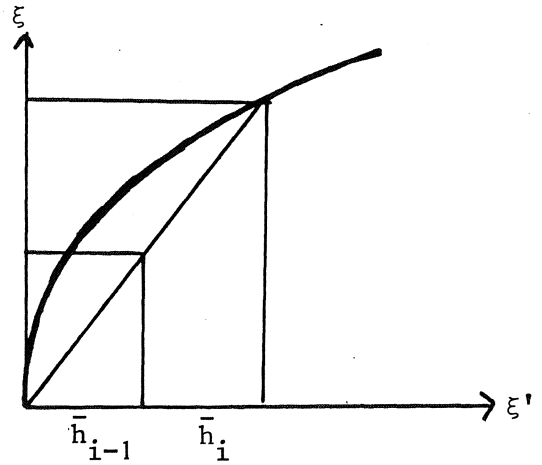


Figure 7.2. Equidistance at a no-slip boundary

The NS equations around the Karman-Trefftz profile after mesh refinement are (2.1.2) with

(7.4) $$A = \frac{d\xi}{d\xi'}, \qquad B = \frac{d\eta}{d\eta'}, \qquad M = a^2 |f'(\bar{\zeta})|^2 e^{2\xi'}.$$

For a certain Reynolds number Re and a mesh size h the coefficients $q_{i,j}$ are large in regions $V^{\ell}_{h,Re} \subset \Omega^{\ell} \cup \partial\Omega^{\ell}$ (because of large $M_{i,j}$ and small $s_0$, see (2.5.4)) and in the neighbourhood of the trailing edge $S_{h,Re} \subset \Omega^{\ell} \cup \partial\Omega^{\ell}$ (because of small $M_{i,j}$, see (2.5.5)). In these regions we have to cut off $q_{i,j}$ and $s_{i,j}$ analogous to (6.6), because otherwise *MULGRI* would diverge. This cutting is justifiable because the vorticity is nearly zero in $V^{\ell}_{h,Re}$ and the streamfunction is nearly zero in $S^{\ell}_{h,Re}$.

In table 7.2 the results are presented for the stretching $V_1 = V_2 = 1$ and $\xi'_{bo} = 1$, $\eta'_{bo} = \pi/4$. In all cases we have to cut off the coefficients $q_{i,j}$ and $s_{i,j}$.

| Re | h | $\nu_0^{(1)}$ | $\nu_0^{(2)}$ | $\nu_0^{(3)}$ | $r_{av}^{(1)}$ | $r_{av}^{(2)}$ | $r_{av}^{(3)}$ |
|---|---|---|---|---|---|---|---|
| 10 | $\pi/6$ | 7 | 6 | 2 | 0.250 | 0.241 | 0.210 |
| | $\pi/10$ | 7 | 5 | 3 | 0.253 | 0.180 | 0.233 |
| | $\pi/18$ | 7 | 6 | 2 | 0.268 | 0.219 | 0.190 |
| 50 | $\pi/6$ | 7 | 5 | 2 | 0.240 | 0.205 | 0.198 |
| | $\pi/10$ | 7 | 6 | 3 | 0.258 | 0.280 | 0.240 |
| | $\pi/18$ | 7 | 5 | 2 | 0.249 | 0.210 | 0.248 |

Table 7.1. Results *MULGRI* applied to the flow around a Karman Trefftz profile with mesh refinement $V_1 = V_2 = 1$, $\xi'_{bo} = 1$, $\eta'_{bo} = \pi/4$. For legenda see table 4.1.

The numbers of iterations in each Newton step are about the same as in the case of no mesh refinement. They are still insensitive to changes in h and to changes in the coefficients induced by Newton iteration.

The figures 7.3, 7.4, 7.5 and 7.6 show the vorticity (multiplicated with a factor 100) around the Karman Trefftz profile at Re = 50, $h = \pi/10$ and with the mesh refinement $V_1 = V_2 = 1$, $\xi'_{bo} = 1$, $\eta'_{bo} = \pi/4$. We see that the boundary layer and the wake nearly coincide with the numerical boundary layer and numerical wake. In point i = 3, j = 6 the boundary layer is about $9/\sqrt{Re}$ and in point i = 8, j = 4 the wake angle is about $6/\sqrt{Re}$.

The figures 7.7, 7.8, 7.9 and 7.10 show the order of magnitude of $c_\xi$ and $c_\eta$ (6.7) in the different parts around the profile. $c_\xi$ and $c_\eta$ are small in the neighbourhood of the trailing edge, $c_\eta$ is small in the numerical wake and $c_\xi$ is small in the numerical boundary layer. It can be concluded that we have to take more mesh points to reduce the remaining $c_\xi$ and $c_\eta$.

In the figures 7.11 and 7.12 the vorticity on the profile is given in the neighbourhood of and far from the trailing edge respectively for Re = 50 and $h = \pi/18$.

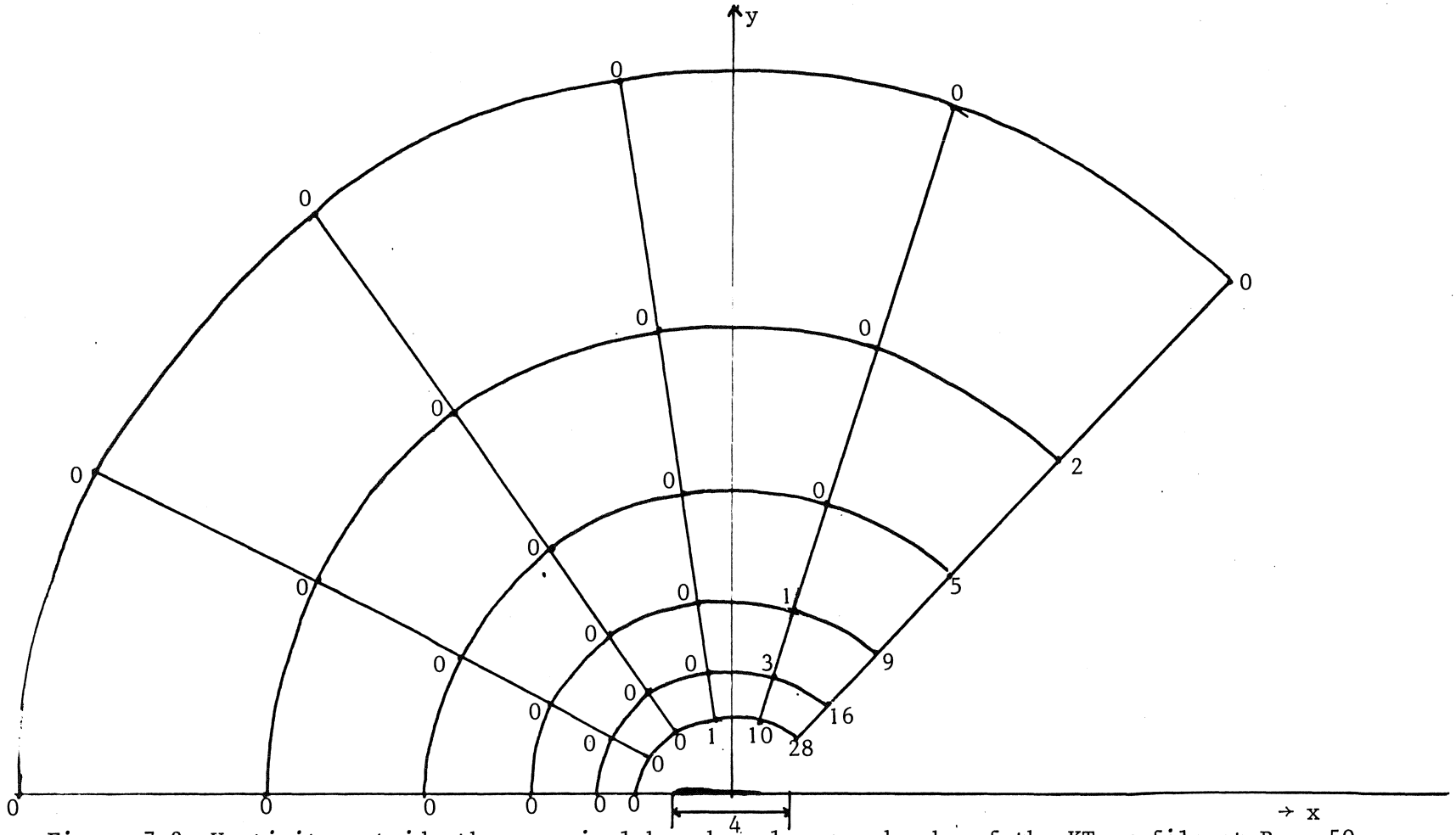


Figure 7.3. Vorticity outside the numerical boundary layer and wake of the KT profile at Re = 50.

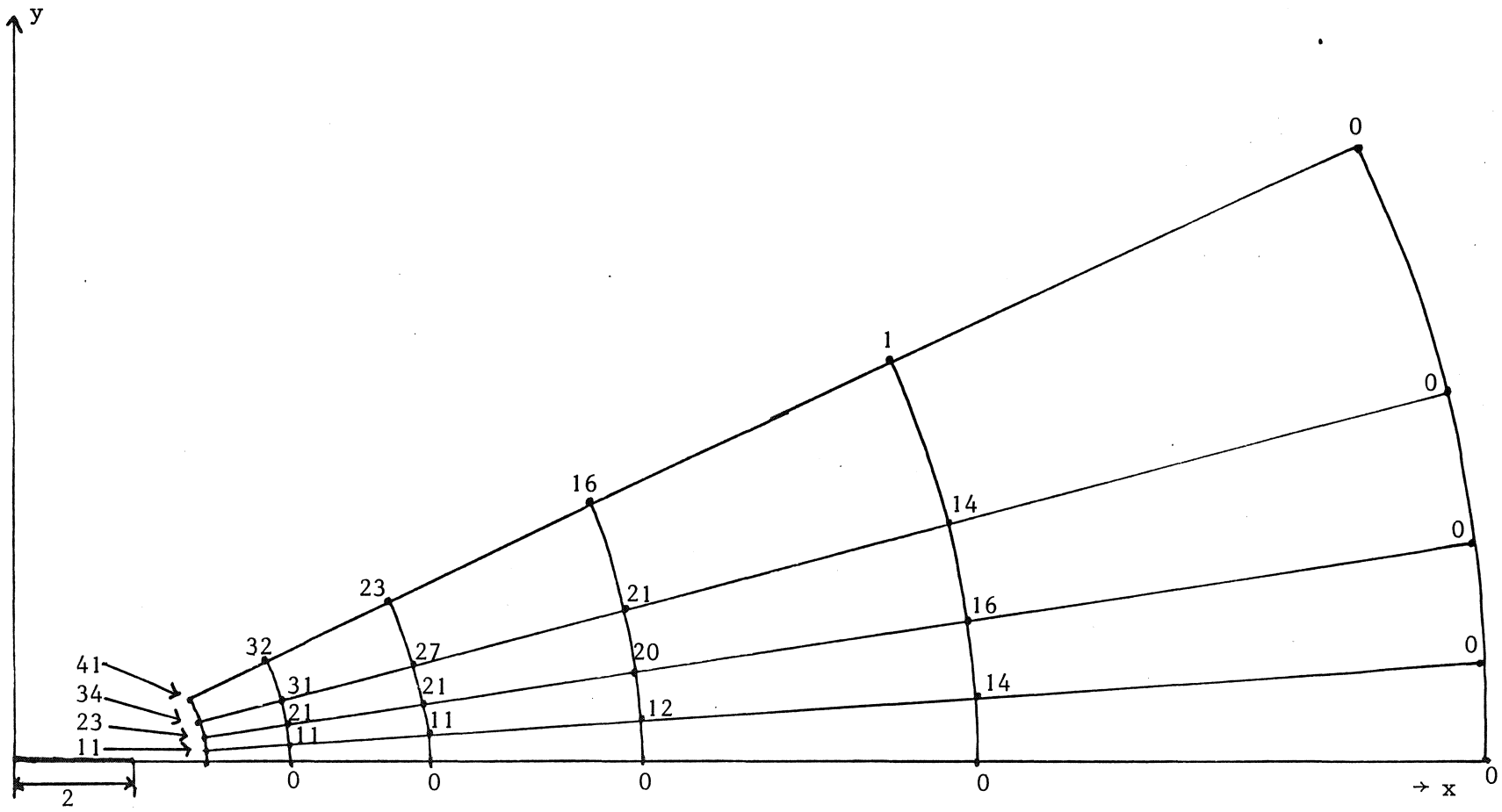


Figure 7.4. Vorticity inside the numerical wake and outside the numerical boundary layer of the KT profile at Re = 50.

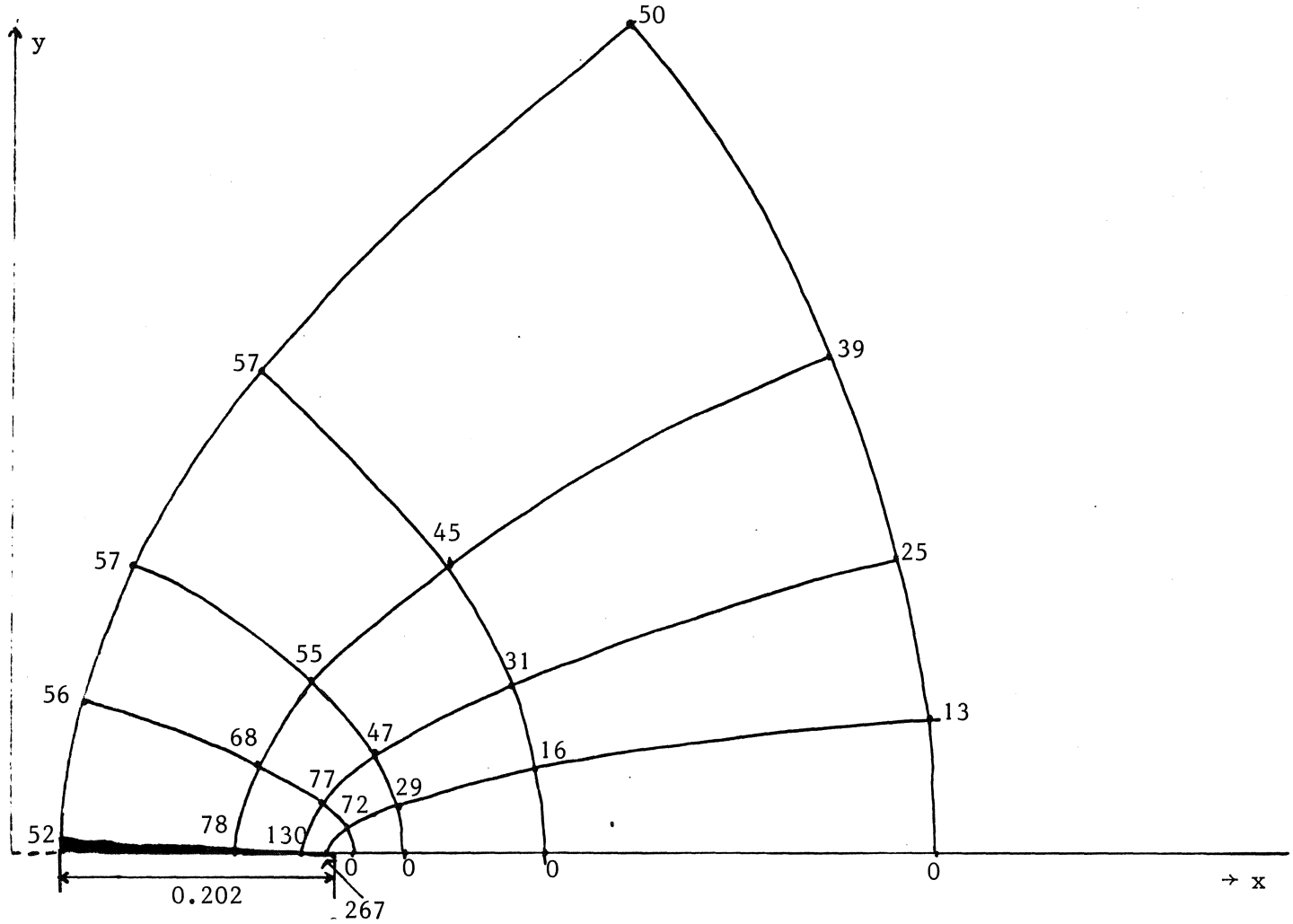


Figure 7.5. Vorticity inside the numerical boundary layer and wake of the KT profile at Re = 50.

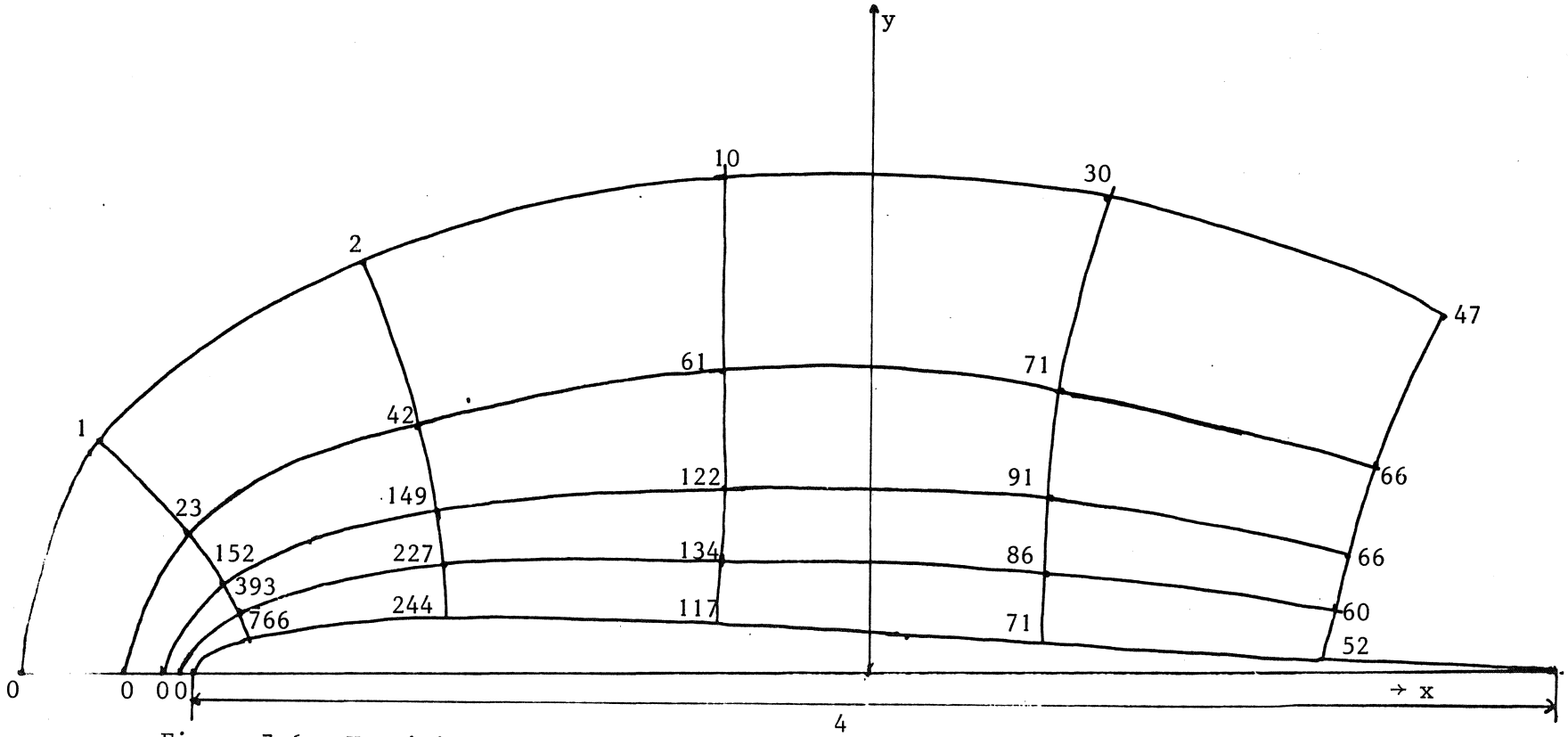


Figure 7.6. Vorticity inside the numerical boundary layer and outside the numerical wake of the KT profile at Re = 50.

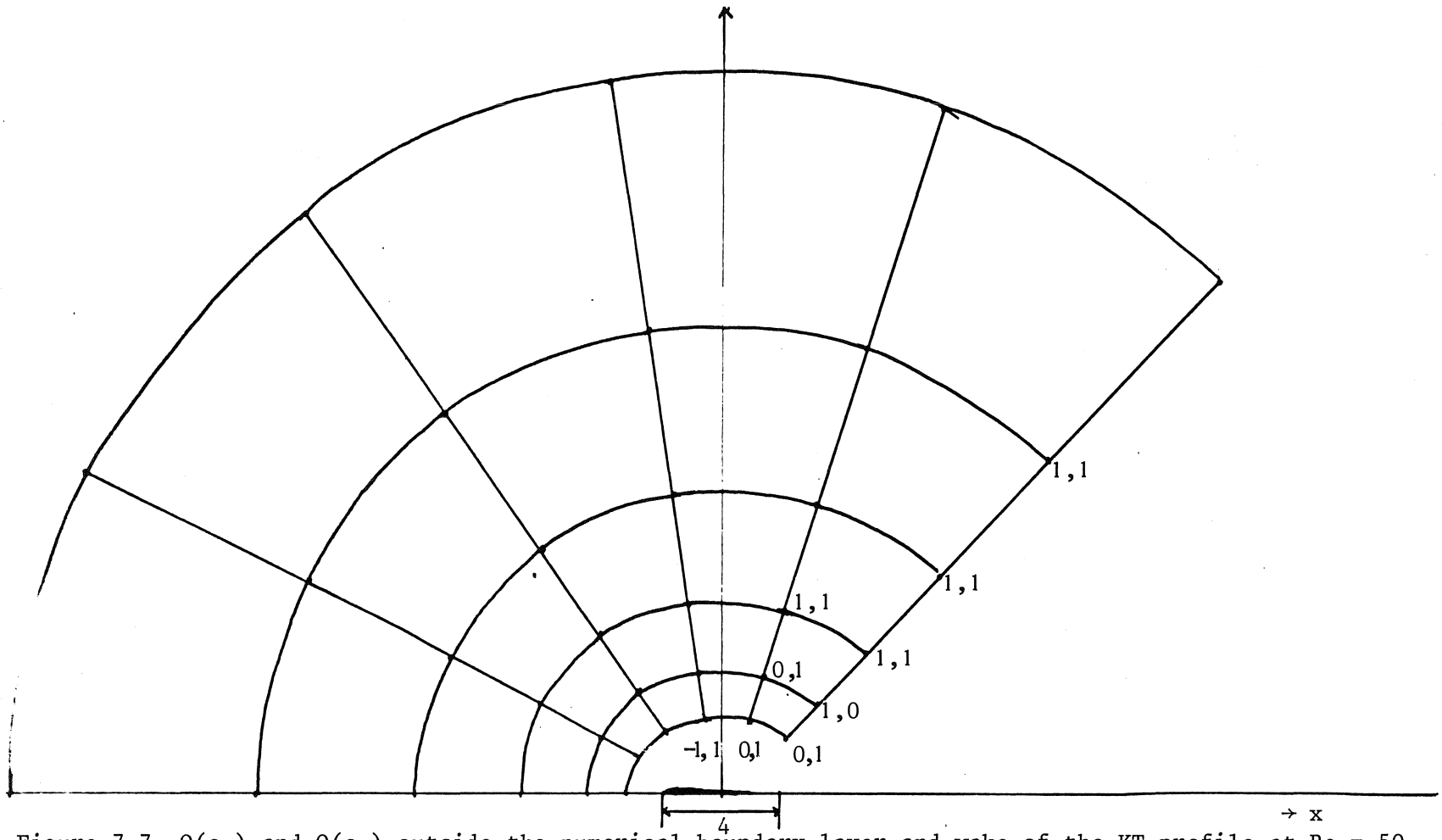


Figure 7.7. $O(c_\xi)$ and $O(c_\eta)$ outside the numerical boundary layer and wake of the KT profile at Re = 50.

For legenda see figure 6.4.

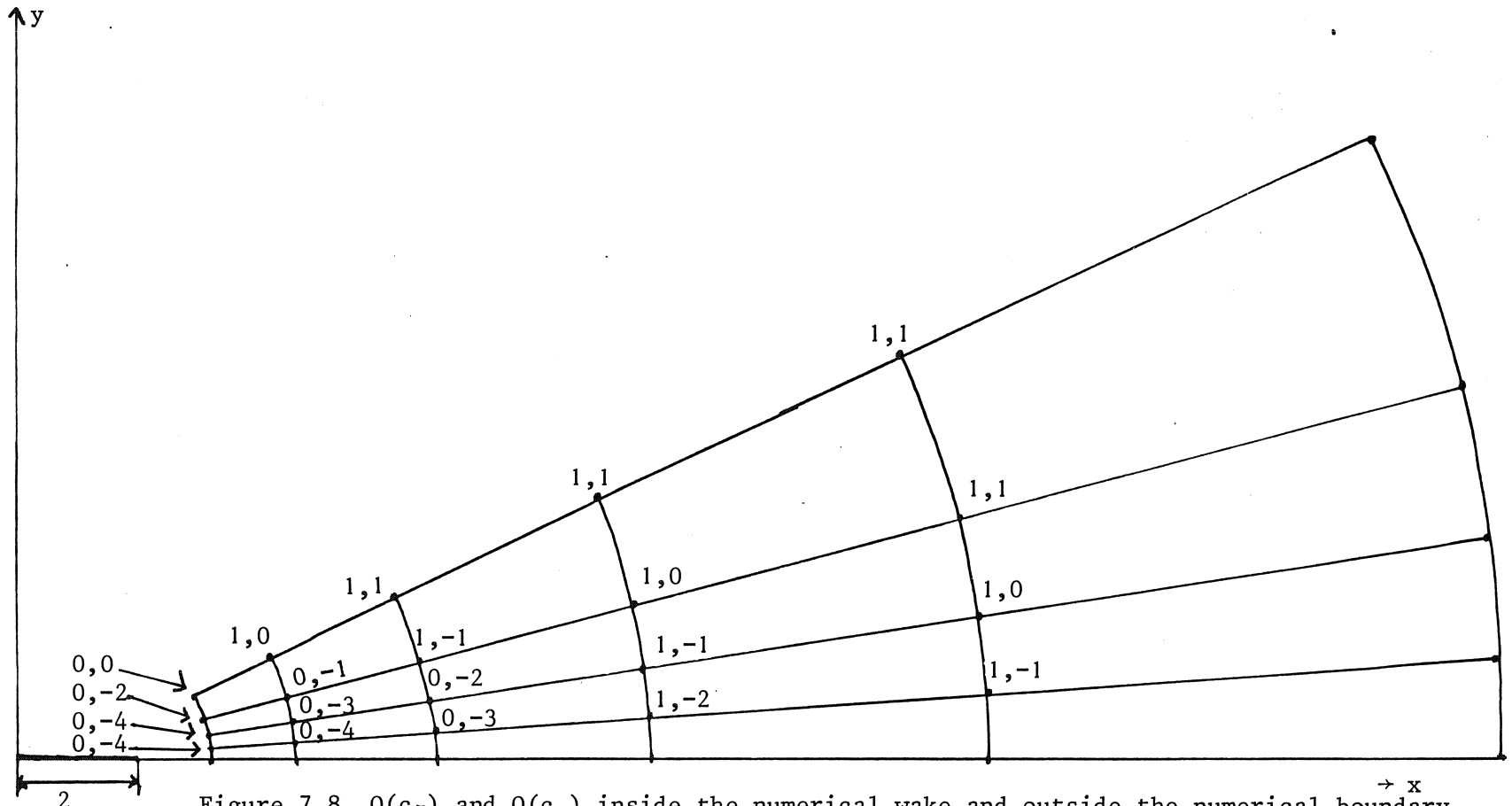


Figure 7.8. $O(c_\xi)$ and $O(c_\eta)$ inside the numerical wake and outside the numerical boundary of the KT profile at Re = 50

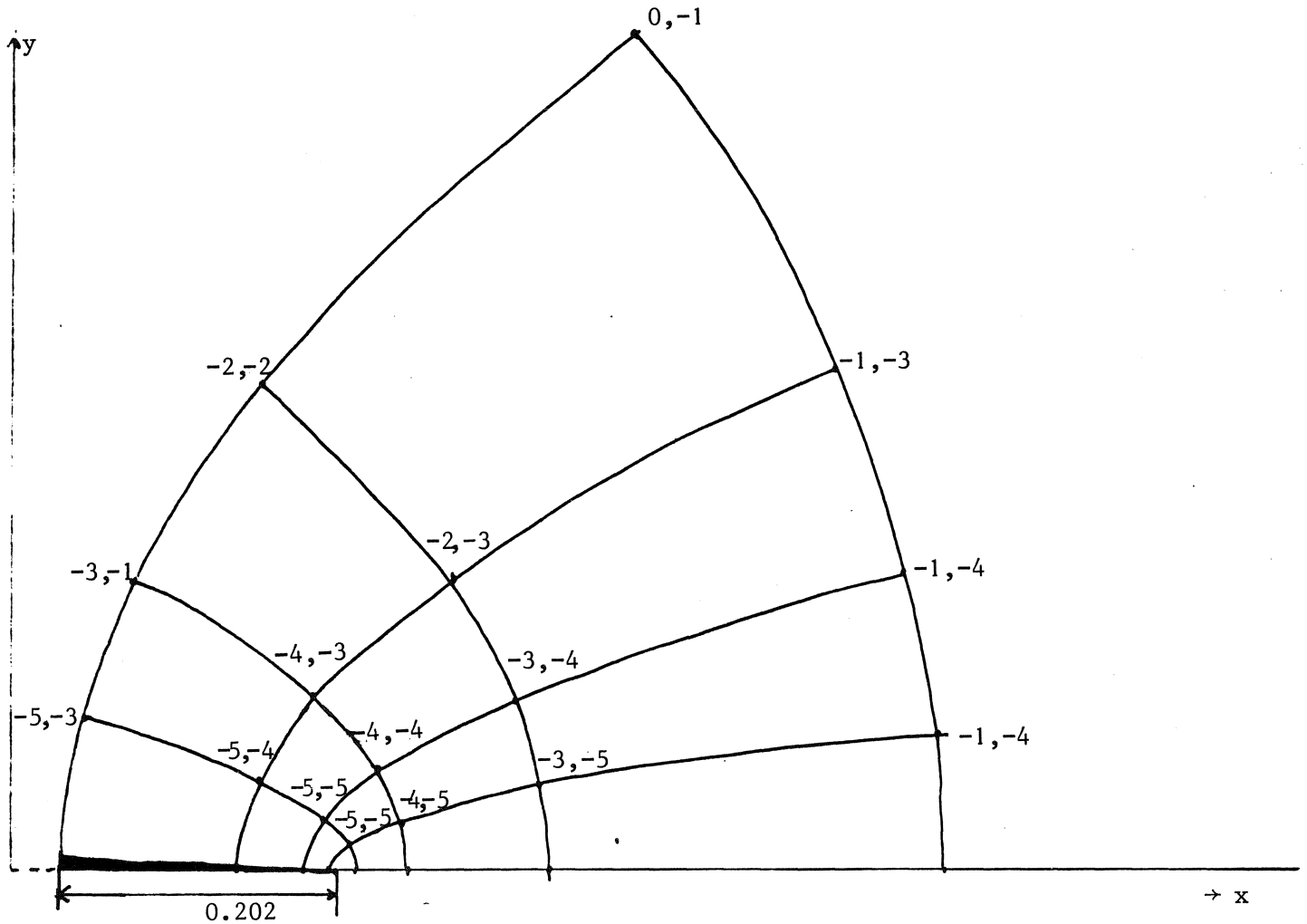


Figure 7.9. $O(c_\xi)$ and $O(c_\eta)$ inside the numerical boundary layer and numerical wake of the KT profile at Re = 50.

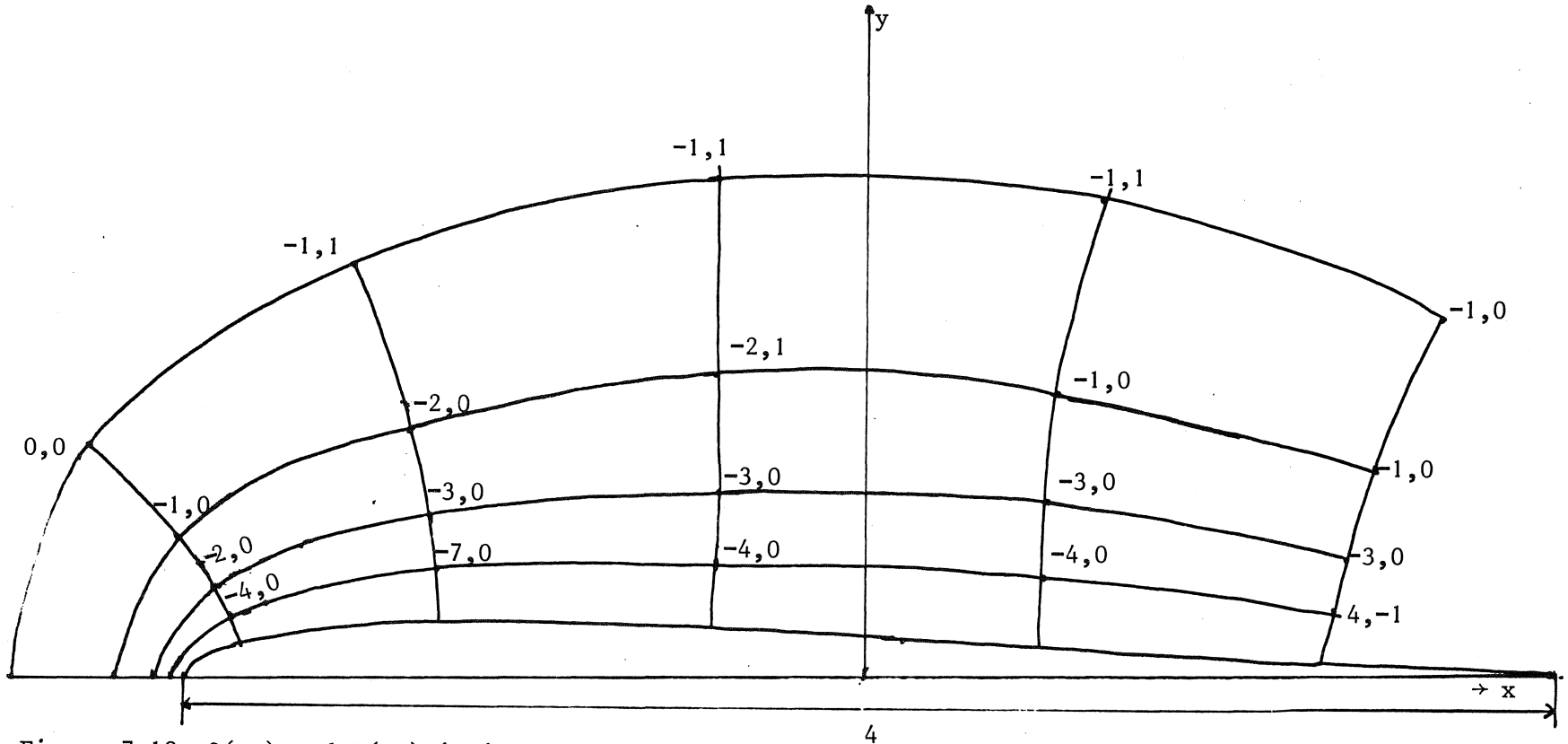


Figure 7.10. $O(c_\xi)$ and $O(c_\eta)$ inside the numerical boundary layer and outside the numerical wake of the KT profile at Re = 50

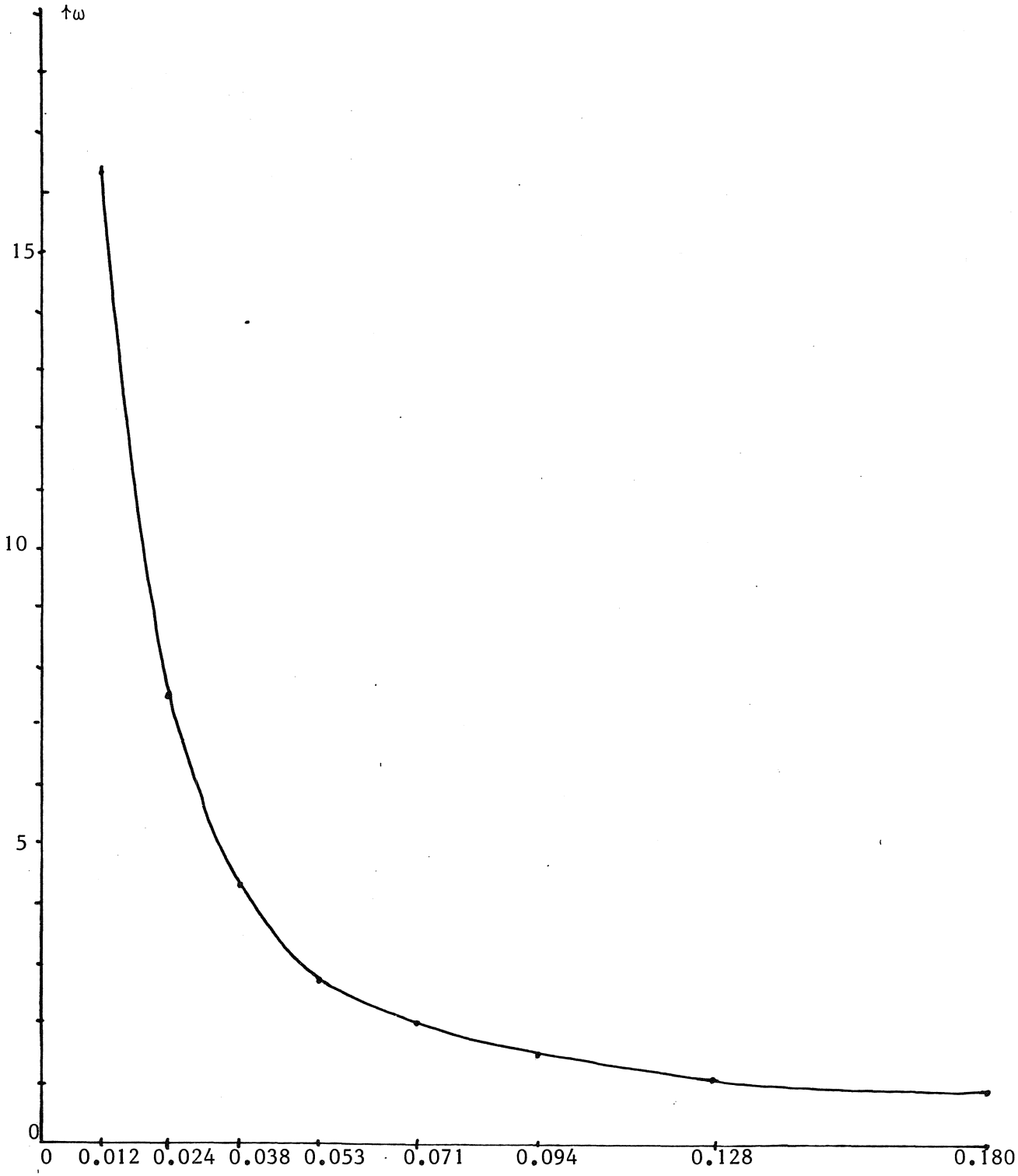


Figure 7.11. Vorticity on KT profile at Re = 50 (h = π/18)

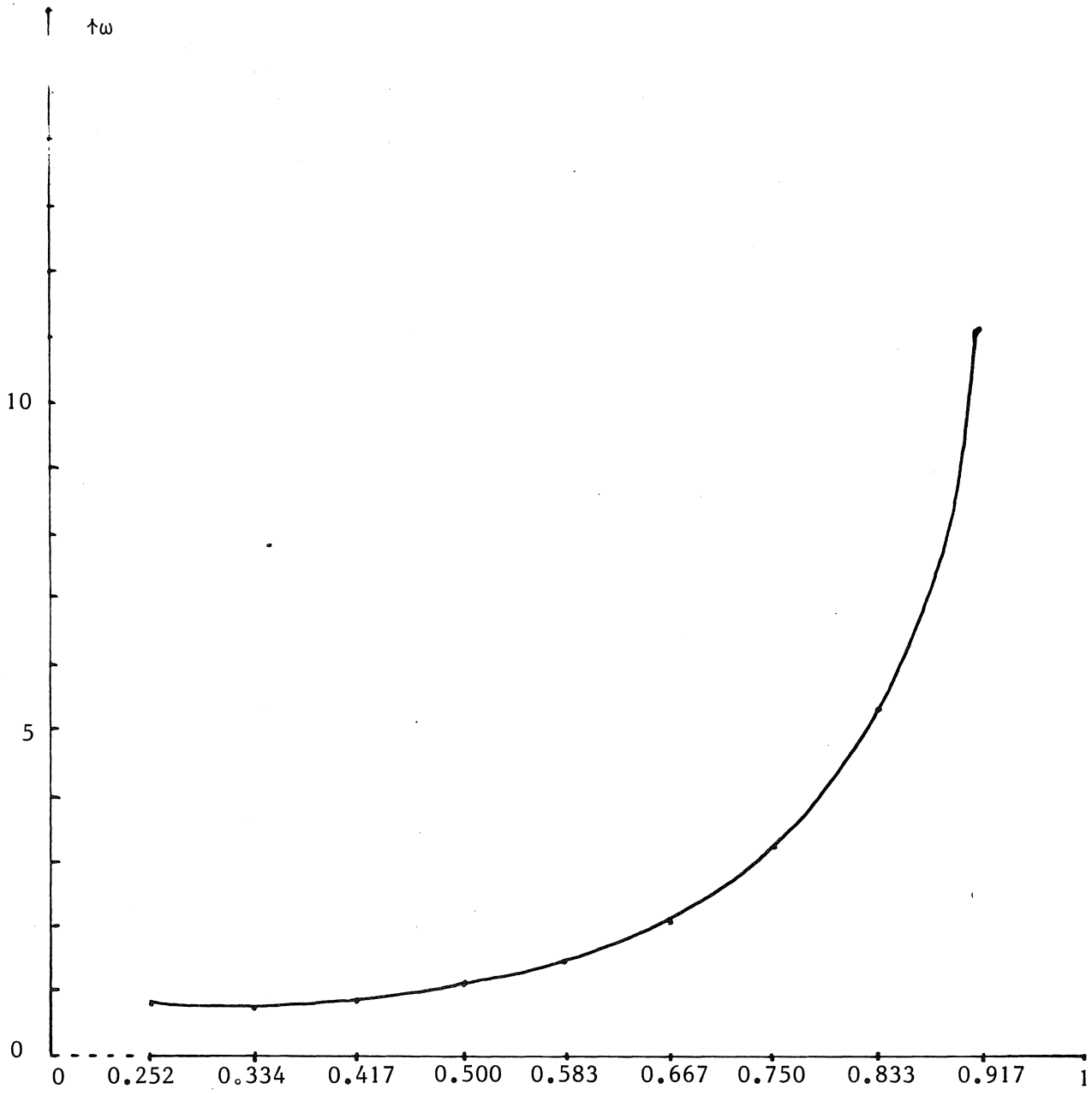


Figure 7.12. Vorticity on KT profile at Re = 50($h=\pi/18$).

## 8. CONCLUSIONS

The multigrid method *MULGRI* (with 9p-ILU, 9p prolongation and restriction, Galerkin coarse grid approximation, 1 coarse grid correction, no smoothing before and 1 smoothing step after correction) is fast and robust in the sense that is also works for the stationary Navier-Stokes equations in a cavity, around a cylinder and around a Karman-Trefftz profile, even with stretched coordinates and relatively large Reynolds numbers. For each problem the number of multigrid iterations in each Newton step is independent of the mesh size h, the changes in the coefficients induced by the Newton iteration and the Reynolds number.

The combination incomplete LU-decomposition and Galerkin coarse grid approximation looks very promising. Especially the ILU smoother, which is based on the simultaneous solving of the $\omega$ and $\psi$ equations, works very well.

Some coefficients in the coefficient matrix of the discretized system of equations may be very large, for instance far from the profile in regions where the vorticity is nearly zero and in the neighbourhood of the trailing edge of the Karman Trefftz profile (where the stream function is nearly zero). Here, the coefficients have to be cut off.

We have shown that the artificial viscosities can be reduced by mesh refinement in boundary layer and wake.

## ACKNOWLEDGEMENT

The author would like to thank Professor P. Wesseling for his constructive remarks and valuable advice.

REFERENCES

[1] v. ASSELT, E.J., *Application of the Osher-Engquist difference scheme and the full multigrid method to a two dimensional non linear elliptic model equation*, Report NW 103/81, Mathematical Centre, Amsterdam (1981).

[2] DENNIS, S.C.R. & CHANG, G.Z., *Numerical solution for steady flow past a circular cylinder at Reynolds numbers up to 100*, J. Fluid Mech. 42, part 3 (1970), 471-489.

[3] IL'IN, A.M., *Differencing scheme for a differential equation with a small parameter affecting the highest derivative*, Math. Notes Acad. Sc. USSR 6 (1969), 596-602.

[4] MOL, W.J.A., *A multigrid method applied to some simple problems*, Memorandum nr 287, Appl. Math. Dept, Twente University of Technology (1979).

[5] MOL, W.J.A., *On the choice of suitable operators and parameters in multigrid methods*, Report NW-107/81, Mathematical Centre, Amsterdam (1981).

[6] MOL, W.J.A., *Smoothing and coarse grid approximation properties of multigrid methods*, Report NW-110/81, Mathematical Centre, Amsterdam (1981).

[7] MOL, W.J.A., *Numerical solution of the Navier-Stokes equations by means of a multigrid method and Newton iteration*, 7th Int. Conf. on Num. Methods in Fluid Mechanics (Stanford 1980), in: Lecture Notes in Physics 141, Berlin & New York (1981), 285-291.

[8] ROACHE, P.J., *Computational Fluid Dynamics*, Hermosa Publishers, Albuquerque (1976).

[9] ROACHE, P.J., *The LAD, NOS and Split NOS methods for the steady-state Navier-Stokes equations*, Computer and Fluids 3 (1975), 179-195.

[10] ROACHE, P.J., *The BID-method for the steady-state Navier-Stokes equations*, Computer and Fluids 3 (1975), 305-320.

[11] TAKAMI, H & KELLER, H.B., *Steady two-dimensional viscous flow of an incompressible fluid past a circular cylinder*, The Physics of Fluids 12, suppl II (1969), 51-56.

[12] TUANN, S. & OLSON, M.D., *Numerical studies of the flow around a circular cylinder by a finite element method*, Computers and Fluids 6 (1979), 219-240.

[13] WESSELING, P., *Numerical solution of the stationary Navier-Stokes equations by means of a multiple grid method and Newton-iteration*, Report NA-18, Delft University of Technology (1977).

APPENDIX A

Consider the nonlinear term $r_{i,j}\omega_{i,j}$:

$$(A.1) \qquad r_{i,j}\omega_{i,j} = \left(\frac{p_{i,j}}{Re} - \frac{\alpha_{i,j}a_{i,j}}{\bar{h}_i} - \frac{\beta_{i,j}b_{i,j}}{\bar{h}_j}\right)\omega_{i,j}$$

The term $\alpha_{i,j}a_{i,j}\omega_{i,j}$ is linearized as follows:

$$(A.2) \qquad \alpha^{\mu+1}_{i,j}a^{\mu+1}_{i,j}\omega^{\mu+1}_{i,j} \cong (\alpha^{\mu}_{i,j} + \alpha'^{\mu}_{i,j}\gamma_{i,j}da^{\mu}_{i,j})(a^{\mu}_{i,j} + da^{\mu}_{i,j}).$$

$$(\omega^{\mu}_{i,j} + d\omega^{\mu}_{i,j}) \cong \alpha^{\mu}_{i,j}a^{\mu}_{i,j}\omega^{\mu}_{i,j} + \alpha^{\mu}_{i,j}a^{\mu}_{i,j}d\omega^{\mu}_{i,j} +$$

$$+ \alpha^{\mu}_{i,j}\omega^{\mu}_{i,j}da^{\mu}_{i,j} + a^{\mu}_{i,j}\omega^{\mu}_{i,j}\alpha'^{\mu}_{i,j}\gamma_{i,j}da^{\mu}_{i,j} =$$

$$= \alpha^{\mu}_{i,j}a^{\mu}_{i,j}\omega^{\mu+1}_{i,j} + (\alpha^{\mu}_{i,j} + \alpha'^{\mu}_{i,j}\gamma_{i,j}a^{\mu}_{i,j})(a^{\mu+1}_{i,j} - a^{\mu}_{i,j}).$$

Therefore, the nonlinear term $r^{\mu+1}_{i,j}\omega^{\mu+1}_{i,j}$ becomes:

$$(A.3) \qquad r^{\mu+1}_{i,j}\omega^{\mu+1}_{i,j} = \left(\frac{p_{i,j}}{Re} - \frac{\alpha^{\mu}_{i,j}a^{\mu}_{i,j}}{\bar{h}_i} - \frac{\beta^{\mu}_{i,j}b^{\mu}_{i,j}}{\bar{h}_j}\right)\omega^{\mu+1}_{i,j}$$

$$- \frac{(\alpha^{\mu}_{i,j} + \alpha'^{\mu}_{i,j}\gamma_{i,j}a^{\mu}_{i,j})\omega^{\mu}_{i,j}(a^{\mu+1}_{i,j} - a^{\mu}_{i,j})}{\bar{h}_i}$$

$$- \frac{(\beta^{\mu}_{i,j} + \beta'^{\mu}_{i,j}\delta_{i,j}b^{\mu}_{i,j})\omega^{\mu}_{i,j}(b^{\mu+1}_{i,j} - b^{\mu}_{i,j})}{\bar{h}_j}.$$

Analogously, the term $r^{\mu+1}_{i+1,j}\omega^{\mu+1}_{i+1,j}$ becomes:

$$(A.4) \qquad r^{\mu+1}_{i+1,j}\omega^{\mu+1}_{i+1,j} = \left(\frac{p_{i+1,j}}{Re} + \frac{(1+\alpha^{\mu}_{i,j})a^{\mu}_{i,j}}{2\bar{h}_i}\right)\omega^{\mu+1}_{i+1,j}$$

$$+ \frac{(1+\alpha^{\mu}_{i,j} + \alpha'^{\mu}_{i,j}\gamma_{i,j}a^{\mu}_{i,j})\omega^{\mu}_{i+1,j}(a^{\mu+1}_{i,j} - a^{\mu}_{i,j})}{2\bar{h}_i}.$$

The terms $r^{\mu+1}_{i-1,j}\omega^{\mu+1}_{i-1,j}$, $r^{\mu+1}_{i,j+1}\omega^{\mu+1}_{i,j+1}$ and $r^{\mu+1}_{i,j-1}\omega^{\mu+1}_{i,j-1}$ are approximated in the

same way.

APPENDIX B

Consider the NS-equations in (u,v,p)-formulation:

$$\text{(B.1)} \qquad \begin{cases} u\dfrac{\partial u}{\partial x} + v\dfrac{\partial u}{\partial y} = -\dfrac{\partial p}{\partial x} + \dfrac{1}{Re}\,\Delta_{xy}\,u \\ u\dfrac{\partial v}{\partial x} + v\dfrac{\partial v}{\partial y} = -\dfrac{\partial p}{\partial y} + \dfrac{1}{Re}\,\Delta_{xy}\,v \\ \dfrac{\partial y}{\partial x} + \dfrac{\partial v}{\partial y} = 0 \end{cases}$$

On a no-slip wall, the equations read :

$$\text{(B.2)} \qquad \begin{cases} \dfrac{\partial p}{\partial x} = \dfrac{1}{Re}\,\Delta_{xy}\,u = \dfrac{1}{Re}\,\dfrac{\partial}{\partial y}\,(\Delta_{xy}\psi) = \dfrac{1}{Re}\,\dfrac{\partial \omega}{\partial y} \\ \dfrac{\partial p}{\partial y} = \dfrac{1}{Re}\,\Delta_{xy}\,v = \dfrac{-1}{Re}\,\dfrac{\partial}{\partial x}\,(\Delta_{xy}\psi) = \dfrac{-1}{Re}\,\dfrac{\partial \omega}{\partial x} \end{cases}$$

From this it can be derived that on the cylinder:

$$\text{(B.3)} \qquad \frac{\partial p}{\partial \eta} = \frac{-1}{Re}\,\frac{\partial \omega}{\partial \xi}$$

The total pressure force in x-direction is:

$$\text{(B.4)} \qquad C_p = \int_0^{2\pi} \frac{-1}{Re}\,\frac{\partial \omega}{\partial \xi}\,\sin\eta\,d\eta = \frac{-2}{Re}\int_0^{\pi} \frac{\partial \omega}{\partial \xi}\,\sin\eta\,d\eta.$$

The skin friktion in a point on the cylinder is

$$\text{(B.5)} \qquad \tau = \frac{\omega}{Re}$$

The total skin friktion in x-direction is

$$\text{(B.6)} \qquad C_f = \frac{2}{Re}\int_0^{\pi} \omega\,\sin\eta\,d\eta.$$

On the for centre line of the cylinder the NS-equations read:

$$\text{(B.7)} \qquad \frac{\partial p}{\partial x} = \frac{1}{Re}\frac{\partial \omega}{\partial y} - u\frac{\partial u}{\partial x}$$

with velocity $u = \frac{-1}{e^{\xi}}\frac{\partial \psi}{\partial \eta}$ . The pressure in the leading edge of the cylinder is

$$\text{(B.8)} \qquad p(\pi) = -\int_0^{\pi} \left(\frac{1}{Re}\frac{\partial \omega}{\partial \eta} - u\frac{\partial u}{\partial \xi}\right) d\xi .$$

The NS equations on the cylinder can be written as (B.3). Thus, the pressure in the trailing edge of the cylinder is:

$$\text{(B.9)} \qquad p(0) = p(\pi) + \int_0^{\pi} \frac{1}{Re}\frac{\partial \omega}{\partial \xi}\, d\eta .$$